La Rivista del Nuovo Cimento (2021) 44:193–249
https://doi.org/10.1007/s40766-021-00018-7

REVIEW PAPER

Nanoscale nonlinear plasmonics in photonic waveguides and circuits

Alessandro Tuniz[1]

Received: 8 December 2020 / Accepted: 24 March 2021 / Published online: 27 April 2021

Abstract

Optical waveguides are the key building block of optical fiber and photonic integrated circuit technology, which can benefit from active photonic manipulation to complement their passive guiding mechanisms. A number of emerging applications will require faster nanoscale waveguide circuits that produce stronger light-matter interactions and consume less power. Functionalities that rely on nonlinear optics are particularly attractive in terms of their femtosecond response times and terahertz bandwidth, but typically demand high powers or large footprints when using dielectrics alone. Plasmonic nanostructures have long promised to harness metals for truly nanoscale, energy-efficient nonlinear optics. Early excitement has settled into cautious optimism, and recent years have been marked by remarkable progress in enhancing a number of photonic circuit functions with nonlinear plasmonic waveguides across several application areas. This work presents an introductory review of nonlinear plasmonics in the context of guided-wave structures, followed by a comprehensive overview of related experiments and applications covering nonlinear light generation, all-optical signal processing, terahertz generation/detection, electro optics, quantum optics, and molecular sensing.

Keywords Nonlinear optics · Plasmonics · Integrated photonics

List of Abbreviations

AZO	Aluminium-doped zinc oxide
CMOS	Complementary metal-oxide-semiconductor
CW	Constant wave
DFG	Difference frequency generation
DMD	Dielectric metal dielectric
EO	Electro-optic

✉ Alessandro Tuniz
alessandro.tuniz@sydney.edu.au

[1] The University of Sydney Nano Institute (Sydney Nano), Intitute of Photonics and Optical Science (IPOS), School of Physics, The University of Sydney, Camperdown, NSW 2006, Australia

ENZ	Epsilon near zero
FOM	Figure of merit
FWM	Four wave mixing
GHPC	Graphene hybrid plasmonic circuit
HNLM	Highly nonlinear medium
HOF	Hybrid optical fiber
HPWG	Hybrid plasmonic waveguide
ITO	Indium tin oxide
LPF	Long pass filter
LR	Long range
MD	Metal dielectric
MDM	Metal dielectric metal
MZM	Mach–Zehnder modulator
NIR	Near infrared
NLE	Nonlinear equation
OR	Optical rectification
PIC	Photonic integrated circuit
PM	Phase matching
PPI	Photonic plasmonic interference
PS	Pulse shaper
SEM	Scanning electron miscroscope
SA	Saturable absorption
SERS	Surface enhanced Raman scattering
SFG	Sum frequency generation
SFWM	Spontaneous four-wave mixing
SHG	Second harmonic generation
SOI	Silicon-on-insulator
SPDC	Spontaneous parametric downconversion
SPM	Self-phase modulation
SPP	Surface plasmon polariton
SR	Short range
THG	Third harmonic generation
UV	Ultraviolet

Contents

1 Introduction

Photonic waveguides are a ubiquitous building block of optical circuits, used from passive long-haul data transfer in optical fibers, to active nanoscale signal processing on miniaturized planar architectures. The idea of using micro-scale circuits to manipulate optical signals from lasers dates back to the 1960s [1], and is now an established and powerful technological platform [2,3]. Such photonic integrated circuits (PICs) now routinely carry, route, and process light via guided waves—using both passive [4] and active [5] components—on a convenient monolithic chip, shown in the Schematic of Fig. 1a. PICs can be implemented using a number of dielectric platforms, including III-V semiconductors [6,7] lithium niobate [8], silicon [3,9] and silicon nitride [10], to name a few—some of which are compatible with complementary metal-oxide-semiconductor (CMOS) fabrication processes [11]. PICs find numerous applications across multiple disciplines [12] including telecommunications [13], quantum technologies [14,15], sensing [16], and machine learning via programmable PICs [5]. Inspired by this approach, optical fibers are also increasingly expanding their traditional guidance capabilities to include active components via metallic, semiconductor, or highly nonlinear materials. A concept schematic of such a hybrid optical fiber (HOF) [17], is shown in Fig. 1b.

The main advantage of waveguide-based PICs over their electronic counterparts is their ability to directly manipulate analogue information that is encoded in photons, which are stable, robust to noise, and have high bandwidth. In recent years, the density of components which perform various functions, shown in the schematic of Fig. 1c, has rapidly increased, up to thousands of photonic components per chip [22], integrated with millions of electronic transistors [23]. Some operations, such as splitting [24], coupling [25], polarization rotation [26], filtering [27], and phase shifting [28], can

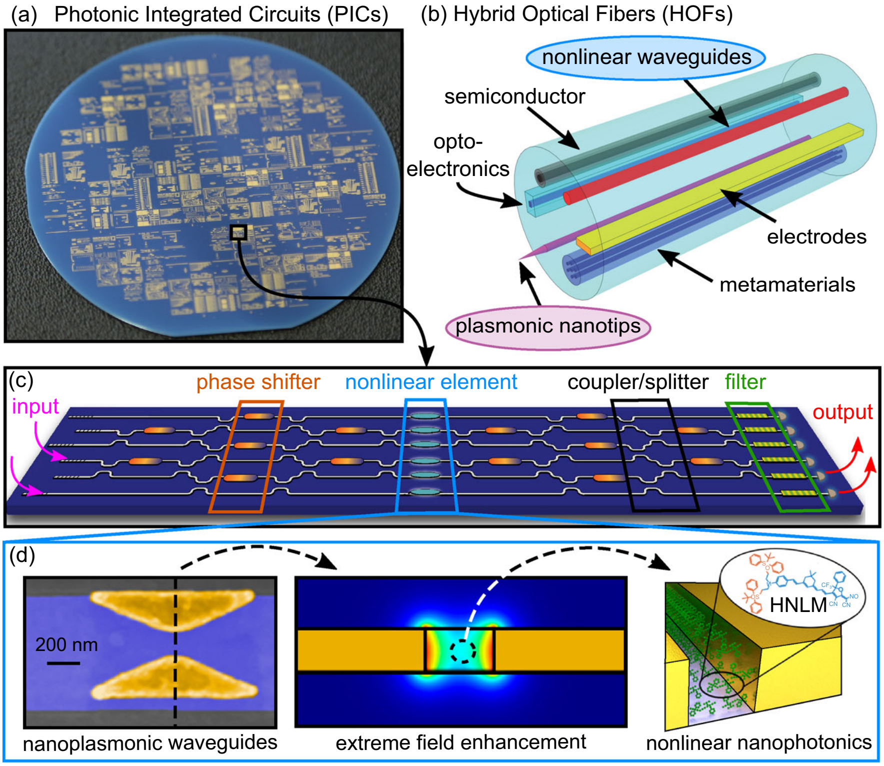

Fig. 1 Photonic waveguide circuit concept schematics. **a** Example centimetre-scale wafer containing densely packed Photonic Integrated Circuits, adapted from Ref. [18] under a Creative Commons License (CC BY-SA 4.0). **b** Hybrid optical fibers (HOFs) can also contain several materials providing all-fiber integrated functions [17], including nonlinear (blue) and plasmonic (purple) waveguides considered in this review. Adapted from Ref. [17] with permission. **c** Schematic example of PIC linear- and nonlinear-elements. Adapted from Ref. [15] with permission (Copyright The Optical Society). In this review, we consider **d** hybrid, guided wave nonlinear plasmonics structures (left) where extreme, nanoscale field enhancements near the metal (middle) can lead to nanometre-scale nanophotonics via highly nonlinear materials (HNLM) [19]. Adapted with permission from Ref. [19] (Copyright The Optical Society) and Ref. [20,21] (Copyright (2018) American Chemical Society)

be entirely passive, agnostic to the amount of power guided by the PIC. In contrast, functions such all-optical switching [29] and light generation [30], are intrinsically active. Since photons do not interact with each other, this manipulation requires an interaction with the optical medium itself, which in its fastest incarnation occurs through the nonlinear optical response at the atomic or molecular level [31].

Although nonlinear responses naturally occur at ultrafast timescales and favour high-bandwidth applications, they are also exceedingly weak, and only become significant for large field intensities. Much effort has been dedicated to finding ways to increase optical nonlinear effects, either by developing new materials with intrinsically high nonlinearities [32] or by appropriately engineering highly nonlinear waveguides [33]. As one perspective describes [34], silica fibers proved to be a valuable platform for many early nonlinear waveguide experiments: although the nonlinearity of silica is low, the development of ultra-low-loss fibers in the 1970s allowed the observation of numerous nonlinear effects including stimulated Raman scattering, self-phase modulation, four-wave mixing and stimulated Brillouin scattering, as well as the first observation of solitons [35] and supercontinuum [36]. All these effects typically require long fiber lengths, and their operational principles crucially rely on the subtle interplay between nonlinear- and dispersive-effects after metres or even kilometres of propagation. In the past decade or so, much effort has thus been dedicated to miniaturizing and integrating these nonlinear functions on readily available chip-scale waveguide elements and circuits composed of highly nonlinear materials such as silicon [37,38] or chalcogenide [32]. Although progress in fabrication has resulted in low linear losses over typical propagation lengths, nonlinear performance is often limited by the materials' *nonlinear* losses (e.g., two-photon- and free-carrier- absorption), though mitigation strategies have been proposed [37].

One obvious advantage of waveguide systems over their bulk counterparts is their ability to maintain a constant spot size upon propagation, via the guided mode: since nonlinear effects demand high field intensities, they are strongest in devices supporting small mode areas. Pushing this concept to its limit, the degree to which any all-dielectric PIC can be miniaturized is inherently restricted to approximately half the wavelength in the medium: if a waveguide lateral dimension falls below this limit, light is no longer tightly confined inside the waveguide and leaks externally [39]. In silicon-based PICs, for example, the lateral dimensions used for guiding telecommunications wavelengths are $\sim 0.5\,\mu\text{m}$. We refer the reader to Ref. [40] for a detailed discussion on important matters relating to all-dielectric nonlinear sub-wavelength photonic circuits.

Truly nanoscale modal confinement can thus only be achieved by using metals: photons can couple to oscillating charges at metallic surfaces, giving rise to surface-plasmon polaritons (SPPs) which can have extremely small effective modal areas—orders of magnitude below the diffraction limit [41]. As such, SPPs have long been eyed as prime candidates for nano-PIC building blocks [42,43]. In this case, holding back immediate uptake is the large *linear* optical loss that accompanies extreme confinement, due to intrinsic electron damping [44]. In the worst case scenario, propagation lengths at metal-dielectric surfaces can be smaller than the wavelength itself. Despite this significant disadvantage, plasmonics continues to attract a lot of attention [45], and is frequently pointed to as the transformative platform for addressing inherent limitations of all-dielectric nonlinear devices [46]. The hope is that, although long-range propagation is out of the question, perhaps local field amplitudes can be large enough to make it all worthwhile. Researchers have thus harnessed *localized* SPPs that oscillate on individual metallic nano-elements without propagating [47]. Indeed, nonlinear plasmonic nanoantennas [48], metasurfaces [49], and metamaterials [50] have all been the subject of intense theoretical and experimental investigations. For overviews of nonlinear plasmonics, we refer the reader to Refs. [51–54]; for a comprehensive review of plasmonics in photonic integrated circuits, we refer the reader to Refs. [55–58].

But what are the prospects for integrating nonlinear plasmonic functionality on a chip for nanoscale nonlinear optics? In first instance, the answer is simple: place a plasmonic element close to a dielectric waveguide [59] and harness the resulting nonlinear process via the localized surface plasmon. Although this approach can enhance the nonlinear performance of dielectric waveguides [59], only a small fraction of total power guided by the dielectric is used. An alternative approach takes a seemingly long-winded route: the diffraction-limited photonic mode can be transformed into a sub-diffraction plasmonic mode (e.g., via a directional coupler [60,61], adiabatic transformers [62,63], or end-fire [64,65] and perpendicular [66–68] couplers), which all guide light to a nano-volume. Photonic-to-plasmonic mode conversion schemes typically require as little as one wavelength of propagation, but still transfer a high fraction of power to a plasmonic nano-concentrator (close to 100%, when combined with mode-matching schemes [65]). For reviews on photonic-to-plasmonic nanocoupling schemes, see for example Refs. [69,70].

Owing to the hybrid nature of the waveguides involved, the vastly different optical properties of each participating material, and the co-existence of two mutually opposing effects (namely, high intensities and large losses), describing the nonlinear effects in plasmonic demands careful consideration. With a number of excellent reviews on nonlinear plasmonics [51,54] and nonlinear metasurfaces [71], here we concentrate on nonlinear plasmonics in guided-wave systems, with an eye on photonic integrated circuits. One example structure, formed by a metal-dielectric-metal nonlinear gap on top of a guiding silicon nanowire, is shown in Fig. 1d: it can produce extreme field enhancements in a guided chip platform, potentially enabling giant nonlinear optics when combined with highly nonlinear materials [19,72,73]. Although not all structures discussed will be on PICs, we have selected theory and experiments which reveal the underlying physics that should be considered in the context of propagating nonlinear SPPs, and is thus relevant to photonic integration.

The outline of this review is as follows. In Sect. 2 we review the linear properties of several representative plasmonic waveguides, and introduce some important parameters impacting their nonlinear performance. In Sect. 3 we give a general overview of nonlinear optics, with particular attention to the Kerr nonlinear response of lossy, hybrid, guided wave systems. We also discuss the relative influence of typical materials, and other nonlinear effects. In Sect. 4 we present salient experiments in guided-wave nonlinear plasmonics. In Sect. 5 we present an experimental overview of photonic-plasmonic nonlinear circuits for nanoscale nonlinear light generation, all-optical switching, electro-optic functions, terahertz generation/detection, and Raman spectroscopy. In Sect. 6 we provide a brief perspective on nonlinear plasmonics in the context of quantum PICs, and conclude in Sect. 7.

2 Fundamentals of plasmonic waveguides

We begin by reviewing the fundamentals of plasmonics waveguides, with particular attention to those parameters that are most relevant for enhancing nonlinear light-matter interactions. With a large number of excellent recent reviews on plasmonic waveguides, we hope to avoid redundancy by concentrating on those parameters most relevant to our later discussion on nonlinear optics: linear propagation loss, group velocity, and effective modal width. In first instance, we can distinguish two common classes of chip-scale plasmonic structures: (1) *pure* plasmonic waveguides, formed

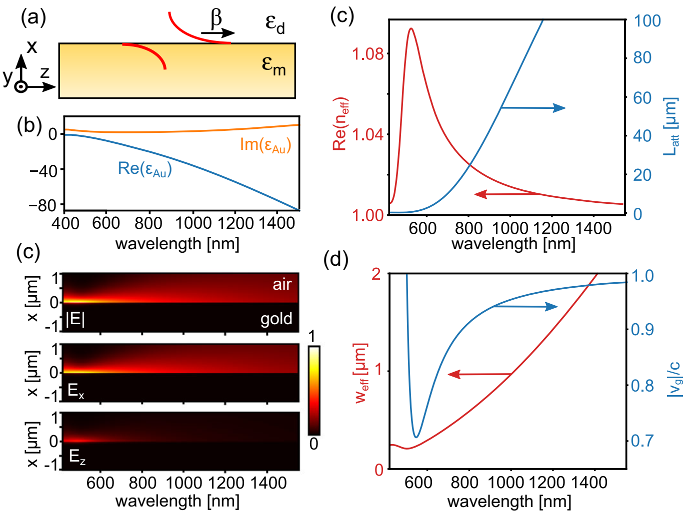

Fig. 2 **a** SPP Schematic. Red line: $\hat{x}$-component of the electric field. **b** Relative electric permittivity ε_m of gold used in the calculations, following the Drude-Lorentz model in Ref. [76]. **c** Effective index n_{eff} (red) and attenuation length L_{att} (blue) of the SPP, assuming $\varepsilon_d = 1$. **d** Colourplot of the electric field norm (top), transverse- ($\hat{x}$, middle) and longitudinal ($\hat{z}$, bottom) electric field components. **d** Calculated w_{eff} (red) and $|v_g|/c$ (blue) versus wavelength, showing minima near $\lambda \sim 600\,\mathrm{nm}$

by one metal and one dielectric; (2) *hybrid* plasmonic waveguides, which harness multiple materials in often sophisticated arrangements, with the ultimate objective of reducing losses and maintaining nanoscale confinement. Unless otherwise stated, in this Section we consider waveguides supporting 1D modes and 2D propagation. This approach allows rapid calculations of both propagation constants and associated modes via numerical solutions of analytical functions [74], retaining much of the underlying physics while reducing the number of degrees of freedom to choose from.

2.1 Pure plasmonic waveguides

The archetypal plasmonic waveguides supporting deep sub-wavelength plasmon modes [75] are the metal-dielectric (MD), the dielectric-metal-dielectric (DMD), and the metal-dielectric-metal (MDM) waveguides. We revisit their most important mode properties, taking the opportunity to compare with their dielectric counterparts where appropriate.

Bulk surface plasmon polaritons (MD)

We start with the simplest plasmonic waveguide, shown in the schematic of Fig. 2a: a semi-infinite metal/dielectric interface supporting a transverse magnetic (TM) surface plasmon polariton (SPP) mode, propagating in z. The dispersion relation of SPP modes has a closed-form expression given by [41]

$$\beta = k_0 n_{\text{eff}} = k_0 \sqrt{\frac{\varepsilon_m \varepsilon_d}{\varepsilon_m + \varepsilon_d}}, \tag{1}$$

where β is the propagation constant, from which the effective index n_{eff} can be obtained via the vacuum wave number $k_0 = 2\pi/\lambda$ (vacuum wavelength: λ), and ε_m (ε_d) are the relative dielectric permittivity of the metal (dielectric). In these calculations, we consider the metal to be gold, one of the most commonly used plasmonic materials as a result of its high stability and relatively low loss, taking the measured values for $\varepsilon_m(\lambda)$ shown in Fig. 2b [76]. Fig. 2c shows the real part of n_{eff} and associated attenuation length $L_{\text{att}} = 1/[2\Im m(\beta)]$ as a function of wavelength. At long wavelengths, ε_m is large and negative, so that $n_{\text{eff}} \sim k_0\sqrt{\varepsilon_d}$. Approaching the visible, $\varepsilon_m + \varepsilon_d \rightarrow 0$ leads to an increase in n_{eff}, limited by material losses via $\Im m(\varepsilon_m)$. Fig. 2d shows a colorplot of the associated electric field magnitude as a function of position and wavelength for modes of equal power: in the near-infrared, the electric field is weakly transversely confined to the metal (metal penetration depth: 20–30 nm); towards visible wavelengths, the field is increasingly confined at the metal/dielectric interface and produces a local intensity enhancement. Note that this effect occurs for both transverse- and longitudinal-field components [77]. We quantify this by calculating the group velocity $v_g = \partial\omega/\partial\beta$ and effective modal width w_{eff}, respectively. Low v_g is associated with slow light [78], which leads to longitudinal enhancement via the trailing edge of a pulse's field catching up with its leading edge; a small effective modal width w_{eff} also enhances the electric field via transverse confinement [79]. The group velocity v_g (normalized to the speed of light c) and w_{eff} (here taken as the $1/e$ width of $|E|$) are shown in Fig. 2d: both have a global minimum close to resonance where $\varepsilon_m = -\varepsilon_d$.

Although the SPP mode is a valuable starting point for the discussion, it approaches a weakly-guided surface wave at longer near-infrared wavelengths where many PICs operate. Field enhancements occur by reducing the waveguide features to subwavelength dimensions, as we now discuss.

Thin metal plasmonic waveguides (DMD)

We now consider the salient properties of modes supported on thin metallic films at the standard telecommunication wavelength $\lambda = 1.55\,\mu\text{m}$ [80]. Here the complex propagation constant is obtained from the numerical solution of an analytical transcendental equation [74]. As the infinite gold film of Fig. 2a transitions into a finite thickness nanofilm, the two supported modes on either side of the film can couple via their evanescent tails, giving rise to anti-symmetric- and symmetric modes (with respect to H), analogously to what occurs for two coupled dielectric waveguides. These are referred to as the short-range (SR-) and long-range (LR-) SPPs, respectively, although other nomenclatures exist [81].

The SR-SPP possesses the most striking characteristics: Fig. 3a shows calculated $\Re e(n_{\text{eff}})$ and associated attenuation lengths L_{att} as a function of film thickness $t = 1-50$ nm. As the phase velocity decreases (large n_{eff}), the losses also increase (short

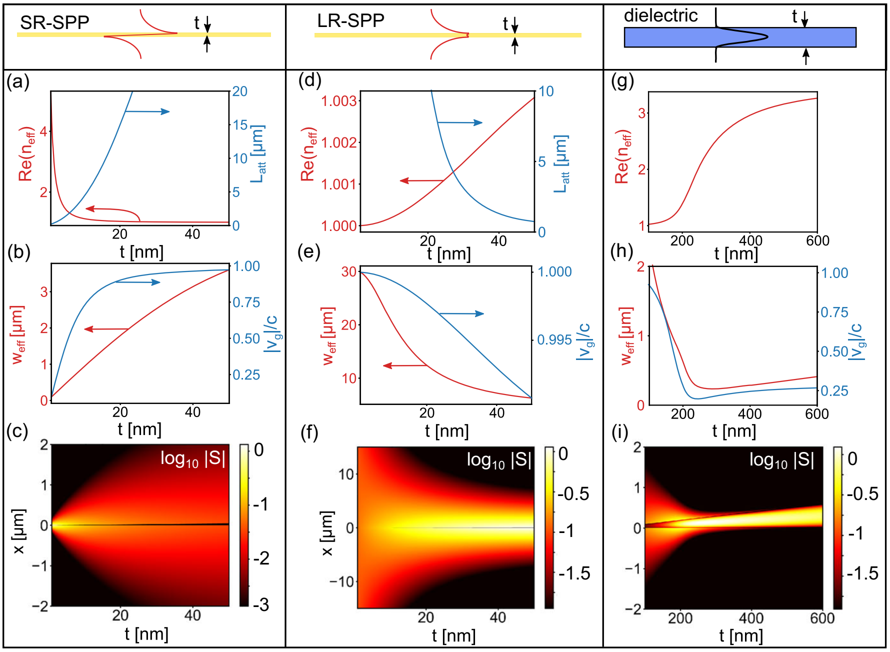

Fig. 3 **a** $\Re e(n_{\mathrm{eff}})$ (red) and attenuation length L_{att} (blue) of the short-range surface plasmon polariton (air/gold/air) as a function of gold film thickness t at $\lambda = 1.55\,\mu\mathrm{m}$. **b** Effective width w_{eff} and group velocity $|v_g|/c$ as a function of t. **c** Colorplot of the Poynting vector magnitude ($\log_{10}|\mathbf{S}|$) as a function of t. **d**–**f** Equivalent calculations for the long-range surface plasmon polariton. **g**–**i** Equivalent calculations for the fundamental mode a silicon slab (air/silicon/air) of thickness t (silicon refractive index: 3.5)

L_{att}). This, in turn, is accompanied by a dramatic reduction in both the w_{eff} and v_g (Fig. 3b) indicating omnidirectional field enhancements at the metal-dielectric boundary as per the SPP. Figure 3c shows the associated Poynting vector magnitude $|\mathbf{S}|$ on a logarithmic scale, illustrating the dramatic increase in confinement of SR-SPPs for nanoscale metal thickness. The increased losses are a direct result of at larger fraction of modal power in the metal, although the largest fraction of power is in the surrounding dielectric. Note that the smallest effective width here corresponds to $\lambda/20$, one order of magnitude below the diffraction limit in free space.

For comparison, Fig. 3d shows that the LR-SPP $\Re e(n_{\mathrm{eff}})$ decreases as the film thickness is reduced, and its attenuation length increases. As Fig. 3e illustrates however, the effective lateral modal width increases to several wavelengths, and v_g/c approaches unity. As the Poynting vector colorplot of Fig. 3f reveals, here the field is not confined to the metal surface as the film thickness is reduced, in sharp contrast to the SR-SPP.

As final comparison, Fig. 3g–i show equivalent calculations for the fundamental mode supported by an all-dielectric air-clad silicon waveguide (refractive index: 3.5; $t = 100{-}600$ nm). Reducing the waveguide width below 100 nm results in an effective index approaching unity (Fig. 3g), and a local minimum in v_g and w_{eff} at $t \sim 200$ nm (Fig. 3h). Though this minimum is associated with field enhancements in the dielectric (shown in the Poynting vector colourplot of Fig. 3i), w_{eff}, v_g, and t are orders of

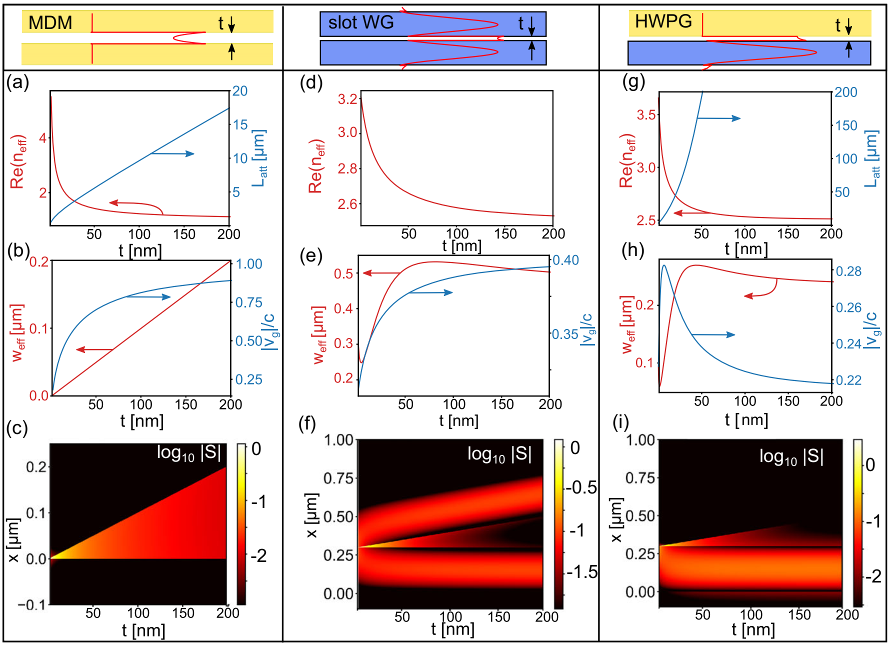

Fig. 4 **a** $\Re e(n_{\text{eff}})$ (red) and attenuation length L_{att} (blue) of the fundamental mode a metal-dielectric-metal (gold/air/gold) waveguide as a function of air gap width t at $\lambda = 1.55\,\mu$m. **b** Effective width w_{eff} and group velocity $|v_g|/c$ as a function of t. **c** Colourplot of the Poynting vector magnitude ($\log_{10} |\mathbf{S}|$) as a function of t. **d**–**f** Equivalent calculations for the fundamental mode of a dielectric slot waveguide (silicon/air/silicon). **g**–**i** Equivalent calculations for the fundamental mode of a hybrid plasmonic waveguide (silicon/air/gold). All calculations are performed with silicon or gold slabs of width $w = 300$ nm

magnitude larger than those of the SR-SPP. The absence of material losses comes at the cost of increased physical dimensions: the relative trade-offs between device footprint and associated losses are a recurring motif when comparing dielectric- and plasmonic-waveguides [43], which is especially relevant for integrated nonlinear plasmonics [82].

Plasmonic slot waveguides (MDM)

The last pure plasmonic strucure we discuss is the plasmonic slot waveguide [83]. We consider the fundamental mode of a sub-wavelength air slot surrounded by two optically thick gold films at $\lambda = 1.55\,\mu$m. Here the gold/air SPP modes on either surface also couple as they are brought together, giving rise to symmetric- and anti-symmetric modes (with respect to the magnetic field): the former produce sub-wavelength lateral confinement and low group velocity.

Figure 4a shows calculated $\Re e(n_{\text{eff}})$ and associated L_{att} of the fundamental MDM mode as a function of sub-wavelength gap thickness ($t = 1$–200 nm): both increase as t approaches the single-nanometre scale, showing a dramatic reduction in both the w_{eff} and v_g, as plotted in Fig. 4b. Figure 4c shows the associated normalized Poynting vector magnitude: the majority of the power remains inside the slot, and the effective width nominally corresponds to the width of the plasmonic gap, which can be orders of magnitude below the diffraction limit. Although a significant portion enters the metal leading to large absorption and short L_{att} (Fig. 4a, blue line), one theoretical study of tapered MDM waveguides [84] showed that, for certain tapering angles, a nonlinear dielectric in the slot could significantly mitigate mode attenuation by exciting a spatial plasmon soliton [85].

A comparable all-dielectric structure is the dielectric slot waveguide [86] shown in Fig. 4d, which uses a high-index dielectric (refractive index: 3.5, $w = 300\,\mathrm{nm}$) instead of gold. The continuity of the displacement field leads to an enhancement of the electric field inside the slot, by a factor corresponding to the ratio of the permittivity of each dielectric [86]. Incorporating a low-index, high-n_2 organic dielectric in a silicon slot can thus already significantly enhance its nonlinear optical properties [87]. Figure 4e shows that w_{eff} and v_g decrease as t approaches nanometre dimensions, and the corresponding intensity colourplot in Fig. 2f indicates that the fraction of the field in the gap also increases. However, relative to the plasmonic slot, the associated field enhancements are orders of magnitude weaker. The extremely low loss of such structures still makes them very attractive for nonlinear applications, but also demand millimetre-scale propagation lengths under typical experimental conditions [87].

2.2 Hybrid plasmonic waveguides

The final relevant structure to consider is the so-called *hybrid plasmonic* waveguide (HPWG) [88–90], shown in the schematic of Fig. 4g: it is formed by a metal structure adjacent to a high-index dielectric, separated by a low-index spacer. This device exhibits properties that are akin to both plasmonic- and dielectric-slot waveguides, retaining some advantages of each when decreasing spacer thickness t. For example, while it possesses a low effective width (here achieving a minimum $w_{\mathrm{eff}} = \lambda/30$, see Fig. 4h), its group velocity does not change as significantly. However, it possesses lower linear losses than the plasmonic slot waveguide, by about one order of magnitude. A colourplot of the field intensity as a function of spacer thickness, shown in Fig. 4i, reveals that much of thie field is in the sub-wavelength low-index spacer. The combination of low losses and large confinement thus makes them candidates for enhancing the nonlinearity of optical waveguides [91].

A "jungle" of plasmonic waveguides

So far we have assumed 1D waveguides and 2D propagation; in practice, any waveguide will have a 2D mode profile and propagate in 3D. As a simple example, cylindrical wires support modes which can be also described by an analytic transcendental equation [92], and the SR- and LR-SPP modes are the radially polarized (TM_0) and linearly polarized (HE_1) modes respectively, each possessing similar properties to those shown in Fig. 3a–f. More complicated profiles demand full calculations [92]. Owing to the large number of associated dimensional and rotational degrees of freedom, there is a vast "jungle" of reported 2D plasmonic waveguide designs, including so-called wedge- [93], channel- [94], gap- [83], and dielectric-loaded [95] plasmonic waveguides, to name a few. All such waveguides form a library of PIC-compatible structures provid-

Fig. 5 Representative 2D modes supported by plasmonic waveguides with sub-wavelength spatial features. These include **a** radially polarized (TM_0) SR-SPPs **b** linearly polarized (HE_1) LR-SPPs on cylindrical nanowires [92], **c** aperture modes [92], **d** gap plasmons [83] **e** dielectric-loaded plasmons [95] and **f** their long-range equivalent [96,97]. Also shown are the modes of **g** a hybrid- [89] **h** channel- [94] and **i** wedge- [93] plasmonic waveguides. *D* dielectric, *L* lower-index dielectric. *A* air, *M* metal. Calculations performed by the Author

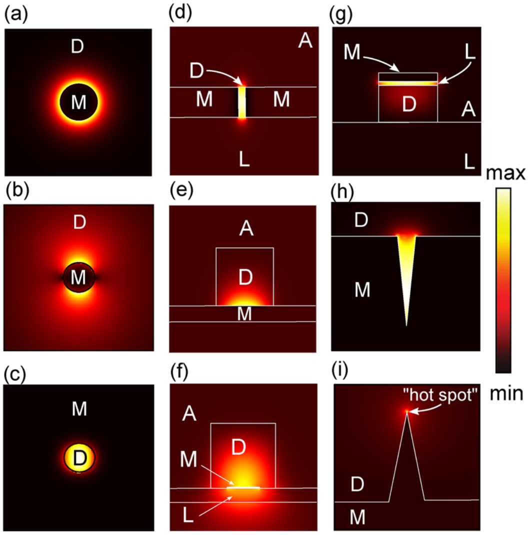

ing omnidirectional field enhancements via their sub-diffraction modes, which in turn strongly depend on the spatial distribution of the higher- and lower-index dielectrics, spacers, and metals involved. A summary figure of commonly reported plasmonic structures and associated modes is shown in Fig. 5. We refer the reader to Ref. [56] for an example review of the linear-modal properties of 2D plasmonic waveguides.

3 Nonlinear optics in lossy media

Having presented the fundamental linear properties of plasmonic waveguides, we now discuss their nonlinear properties, which began attracting increased attention starting in the 1980s [98,99]. We first review some relevant theoretical tools and results, and begin considering the simple textbook case [31,51] of a homogeneous, isotropic material, which responds to a scalar electromagnetic field E via a polarization

$$P = \varepsilon_0 \left[\chi^{(1)} E + \chi^{(2)} E^2 + \chi^{(3)} E^3 + \ldots \right], \tag{2}$$

where ε_0 is the permittivity of vacuum and $\chi^{(n)}$ is the material's n-th order electric susceptibility. More generally, this expression can contain E oscillating at different frequencies ω_i to produce a polarization $P(\omega)$, in which case $\chi^{(n)}$ depends on the frequencies involved. Since electric and polarization fields are most generally vectors, $\chi^{(n)}$ are generally tensors. Linear optical processes (e.g, refraction and absorption) are described by the $\chi^{(1)}$ term in Eq. (2) alone, valid for small field amplitudes, and involving one frequency at a time. Optical processes at larger field amplitudes can only be described by including higher-order terms, which result in more complicated interactions involving multiple frequencies. $\chi^{(2)}$ is responsible for several important effects such as second harmonic generation (SHG), optical rectification (OR), and sum/difference frequency generation (SFG/DFG); $\chi^{(3)}$ can give rise to even more nonlinear processes, but the most commonly considered are the Kerr effect, third-harmonic generation (THG), four-wave-mixing (FWM), self-phase modulation (SPM). All these effects are described in great detail in several textbooks [31,80] and reviews [51,54].

Since $\chi^{(2)}$ nonlinear processes are prohibited in centro-symmetric structures, in the context of plasmonic waveguides they most commonly occur at metal/dielectric interfaces where centro-symmetries are trivially broken [100], although many plasmonic waveguide designs also include non-centrosymmetric structures adjacent to the metal [19,101]. In contrast, all materials have non-zero third-order susceptibility, making $\chi^{(3)}$ effects always relevant at high intensities. The most important third-order nonlinear process is arguably the Kerr effect, which is responsible for the nonlinear polarization at the incoming frequency. We now consider it in some detail, with particular attention to hybrid waveguide structures containing lossy materials.

3.1 The nonlinear Kerr coefficient

A plane wave with wavenumber $k = nk_0$ propagating in a bulk medium with complex refractive index n, induces a nonlinear refractive index change in the medium at high intensity I. The nonlinear refractive index n_2 quantifies the change in refractive index per unit intensity:

$$n = n_0 + \Delta n(I) = n_0 + n_2 I, \tag{3}$$

where $n_0 = \lim_{I\to 0} n$ is the linear refractive index. For bulk lossy materials, n_2 is related to $\chi^{(3)}$ via [31,102]

$$n_2 = \frac{3\chi^{(3)}}{4n_0 \Re e(n_0)\varepsilon_0 c}, \tag{4}$$

and is most commonly measured using the z-scan technique [103].

With knowledge of materials' n_0 and n_2, we now consider multi-material waveguides that support modes with propagation constant $\beta = n_{\text{eff}} k_0$ and power P. In this case, the change in propagation constant is quantified by a nonlinear coefficient γ via

$$\beta = \beta_0 + \Delta\beta = \beta_0 + \gamma P, \tag{5}$$

where $\beta_0 = \lim_{P\to 0} \beta$ is the linear propagation constant.

The parameter γ is required to simulate high-intensity light propagation in waveguides using a nonlinear equation (NLE) [80]. In the simple case of extremely lossy waveguides with short, wavelength-scale propagation distances, the NLE is given by

$$\frac{\partial A}{\partial z} + \frac{\alpha_0}{2} A = i\gamma |A|^2 E, \tag{6}$$

where $\alpha_0 = 2\Im m(\beta_0)$ is the linear absorption coefficient of the waveguide, and A is a field amplitude. Note that γ is a complex number—its real part is associated with

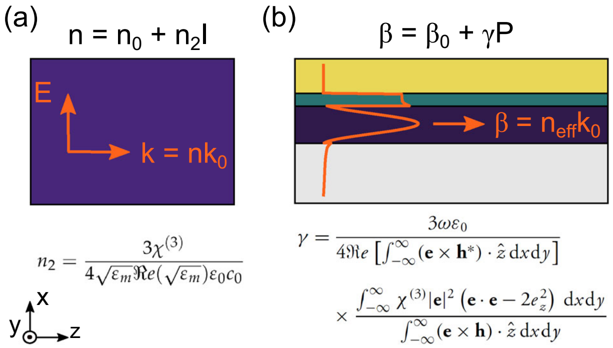

Fig. 6 Concept schematic of the nonlinear refractive index n_2 and nonlinear coefficient γ. **a** Bulk medium with linear refractive index n_0 and nonlinear refractive index n_2. A plane wave of intensity I changes the refractive index by $n_2 I$, following Eq. (4). **b** Waveguide composed of arbitrary lossy media supporting a mode with a linear propagation constant β_0, power P, and electric- and magnetic-vector fields $\{\mathbf{e}, \mathbf{h}\}$. The propagation constant changes by γP following Eq. (7). Note that $\chi^{(3)}$ is a function of transverse position

the nonlinear phase shift, and its imaginary part is associated with optical limiting or saturable absorption. Generalizations of Eq. (6) may contain additional nonlinear or dispersive effects [36], and can be extended to describe extended coupled pump, signal, and idler fields [82]. Equation (6) can also be generalized to include the transverse field dependence [104], which is necessary to describe plasmon-solitons whose spatio-temporal profile does not change with z even in a transversely infinite medium due to self-focusing effects [85].

Parameters n_2 and γ are analogous in that their real parts give the nonlinear phase shift and their imaginary parts give rise to optical limiting or saturable absorption, depending on sign. Calculating γ is generally difficult, especially in waveguides formed by multiple, high-index materials that induce optical losses. In the simple case of low-loss single mode optical fibers with low index contrasts, which possess similar n_2 in the core and cladding and support scalar modes, $\gamma = k_0 n_2 / A_{\text{eff}}$ where A_{eff} is an effective mode area [36]. Until recently, it remained unclear which of the many expressions for γ [105–109] were valid for hybrid waveguides formed by extremely lossy materials. Following a systematic analysis and comparison with full numerical calculations, the most general expression for γ was ultimately established to be [110]

$$\gamma = \frac{3\omega\varepsilon_0}{4\Re e\left[\int_{-\infty}^{\infty}(\mathbf{e}\times\mathbf{h}^*)\cdot\hat{z}\,dxdy\right]} \frac{\int_{-\infty}^{\infty}\chi^{(3)}(x,y)|\mathbf{e}|^2\left(\mathbf{e}\cdot\mathbf{e}-2e_z^2\right)\,dxdy}{\int_{-\infty}^{\infty}(\mathbf{e}\times\mathbf{h})\cdot\hat{z}\,dxdy}, \qquad (7)$$

where $\mathbf{e}$, $\mathbf{h}$ are electric- and magnetic-modal fields respectively, ω is the angular frequency, $\hat{z}$ points in the propagation direction, and the xy plane is transverse. Equation (7) was independently obtained by Im et al. [111] and Li et al. [109], and although it appears complicated, it can be immediately calculated using any linear mode solver, requiring only knowledge of the linear- and nonlinear- properties of an arbitrary waveguide's constituent materials.

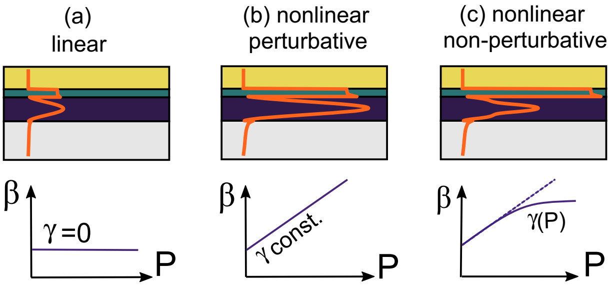

Fig. 7 Schematic comparing perturbative and non-perturbative approaches. **a** In the linear regime, β is constant and $\gamma = 0$. In the nonlinear regime, P increases the propagation constant by γP. **b** In perturbative treatments, the nonlinear permittivity changes but the mode profile is assumed not to and γ is constant. **c** In non-perturbative treatments γ depends on P. Orange line: intensity. Adapted from Ref. [110]

Equation (7) reduces to Eq. (39) in Ref. [108], valid for arbitrary lossless waveguides, and can factorized in terms of more physically intuitive properties [77,79]. This factorization is not unique: one choice, shown to be valid for lossless waveguides, is given by [91]

$$\gamma = k_0 \left(\frac{c}{v_g}\right)^2 \frac{\overline{\chi}^{(3)}}{A_{\text{eff}}}, \tag{8}$$

where $\overline{\chi}^{(3)}$ is the average of nonlinear susceptibility over the constitutive materials, weighted by the magnitude of the electric field. The definition of effective area A_{eff} is also not unique [79]: one frequently used choice is given by the area of longitudinal power flow [108]

$$A_{\text{eff}} = \frac{|\int_{\infty}^{\infty} (\mathbf{e} \times \mathbf{h}^*) \cdot \hat{z}\, dxdy|^2}{\int_{\infty}^{\infty} (|\mathbf{e} \times \mathbf{h}^*|^2) \cdot \hat{z}\; dxdy}. \tag{9}$$

The factorization of Eq. (8) provides valuable physical intuition: v_g enhances the transverse electric field due to slow-light effects, and A_{eff} gives rise to longitudinal field enhancement. Both can drive nonlinear changes in the refractive index of the waveguide's constituent materials, modifying the propagation constant. A similar factorization was recently shown to provide useful insights even for extremely lossy plasmonic waveguides [77]. With the factorization of Eq. (8), we can go back and estimate that the SR-SPP and MDM structures of Figs. 3b and 4b would possess the largest γ amongst the structures considered in Sect. 2, although material properties also play an important role via $\overline{\chi}^{(3)}$.

Note that both Eqs. (4) and (7) consider nonlinear changes in the refractive index to be small perturbations, so that the propagation constant of the mode changes but the fields do not, as illustrated in the schematics of Fig. 7a, b. For large relative nonlinear index changes, non-perturbative approaches are necessary [112], which account for changes in both the optical medium and the modal profile [113] as illustrated in the schematic of Fig. 7c. This results in a power-dependent γ [110,113–115]. This compli-

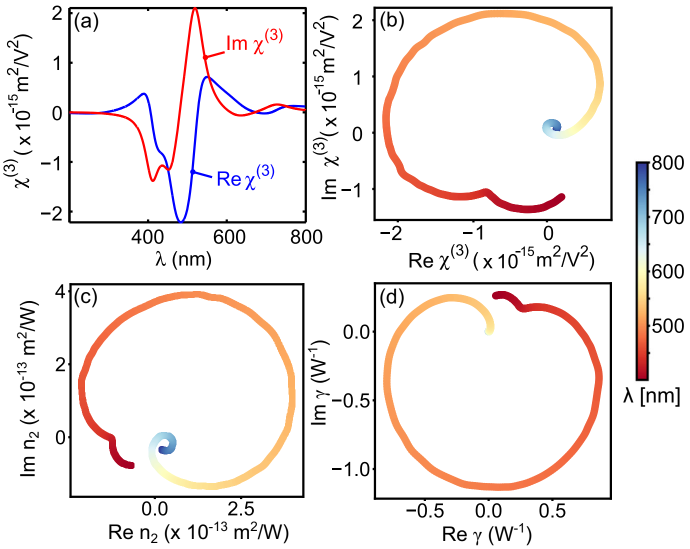

Fig. 8 Complex nonlinear susceptibility $\chi^{(3)}$ of gold **a** as a function of wavelength [105] and **b** plotted in the complex plane [110]. **c** Associated gold n_2 [Eq. (4)] plotted in the complex plane. **d** Associated SPP γ [Eq. (7)] plotted in the complex plane. Note the scaling and rotation of gold n_2 and SPP γ with respect to gold's $\chi^{(3)}$. Colourbar represents wavelength. **a** is adapted from Ref. [105] under a creative commons license (CC BY-NC-SA 3.0)

cated nonlinear problem can be addressed by numerically iterating a series of simple linear problems [114]: the calculated linear mode at a given power changes the local refractive index, resulting in a graded index profile supporting a new mode, which is then calculated. This process can be iterated until the propagation constant converges, although this is not guaranteed. The change in propagation constant $\Delta\beta(P)$ is linear only at low powers as shown in Fig. 7c, and the nonlinear coefficient of Eq. (7) is given by $\gamma = \lim_{P\to 0} d\beta/dP$. At sufficiently high powers, local changes in the materials' refractive index can be strong enough to induce modal bifurcations, for example in nonlinear plasmonic slot waveguides [116,117]. Non-perturbative approaches have recently emerged to interpret experiments in so-called epsilon-near-zero materials [112], which exhibit extremely large nonlinear refractive index changes [118] and are increasingly relevant for ultra-compact nonlinear devices applications [77,119]—see also Sect. 4. Unless otherwise stated, all present discussions relate to non-perturbative conditions.

3.2 Relating $\chi^{(3)}$ and γ: a complex matter

The relationship between complex n_2 and complex $\chi^{(3)}$ for bulk media has some interesting and counter-intuitive consequences [120]. To illustrate this, we consider the $\chi^{(3)}$ dispersion for gold, theoretically considered in Ref. [105] and shown in Fig. 8a. The wavelength dependence of $\chi^{(3)}$ can also be represented in the complex plane as shown in Fig. 8b. Equation (4) then indicates a rotation of n_2 with respect to $\chi^{(3)}$ in the complex plane, as shown in Fig 8c. The analytical relation between γ and $\chi^{(3)}$ for arbitrary plasmonic waveguides is not so simple, although for the case of a SPP γ can be calculated analytically [110], and is shown graphically in Fig. 8d.

In waveguides with no linear loss, i.e. when the linear permittivity is purely real, the real part of γ is proportional to $\Re e\left[\chi^{(3)}\right]$ and the nonlinear absorption is proportional to $\Im m\left[\chi^{(3)}\right]$. However, this proportionality fails for lossy waveguides, i.e. when the linear permittivity is complex. Indeed, note that γ can be purely real, corresponding only to a nonlinear phase shift and no nonlinear absorption, even when both real and imaginary parts of $\chi^{(3)}$ are negative. Similarly, γ can be purely imaginary, i.e. only nonlinear absorption and no nonlinear phase shift, even when both real and imaginary parts of $\chi^{(3)}$ are positive. Figure 8 also demonstrates that there is no straightforward correlation between the complex phase of γ and that of $\chi^{(3)}$, and that the full complex nature of both the linear and nonlinear quantities plays an important role both in bulk metals [102,120,121] and in plasmonic waveguides [110,111].

3.3 Figures of merit of Kerr nonlinear performance

With knowledge in hand of both linear losses and nonlinear coefficients, we now consider the nonlinear performance of Kerr plasmonic waveguides, and discuss how figures of merit can guide their designs. Since attenuation lengths in plasmonic waveguides are quite short—typically a few wavelengths, see for example Fig. 3a—phase matching (PM) is not as crucial as for low-loss systems. This can be understood by examining Fig. 9, which schematically illustrates how much nonlinear power P_{NL} is generated by a driving pump under different conditions. Phase matching (blue curve) leads to the phase fronts of the pump- and nonlinear-fields to advance synchronously, and the nonlinear fields to add up coherently upon propagation, conserving momentum. PM is crucial in for the efficient build-up of nonlinear power over optically long distances, because the nonlinear response of dielectric materials is weak, and high conversion efficiencies require careful design [31]. In the absence of phase matching (red curve), the resulting nonlinear fields can have different relative phases during propagation, which limits the amount of nonlinear power produced. In extremely lossy plasmonic systems, absorption has the effect of both reducing pump power at long lengths (preventing nonlinear light generation), and attenuating the intensity of the generated nonlinear signal (removing the generated signal). In this scenario, the phase matching requirement is moot, since at long lengths loss is the dominant mechanism limiting nonlinear effects. This is more quantitatively highlighted by full calculations of conversion efficiencies for the specific case of near-degenerate four wave mixing in the lossless- and lossy-case, shown in Fig. 9b, c respectively [82].

An important quantity to consider in Kerr nonlinear waveguides is the nonlinear phase shift $\Delta\phi_{\mathrm{NL}}(t)$, induced by changes in the propagation constant at high powers, as described by Eq. (5). In the case of a temporally varying ultrashort optical pulse of power $P(t)$ centered around a frequency ω_0 propagating inside a lossy medium, the

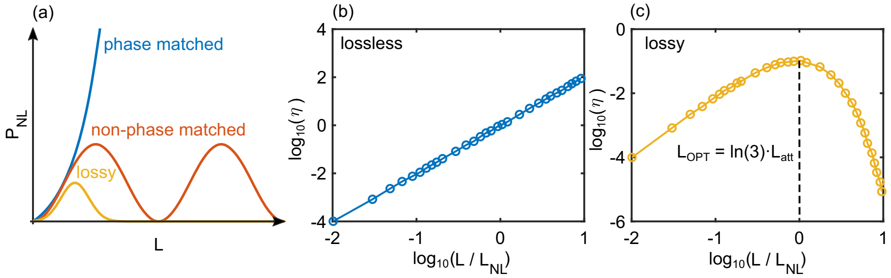

Fig. 9 **a** Schematic showing the power generated by nonlinear effects P_{NL} as a function of propagation length L at different regimes: phase-matched lossless systems yield increasing P_{NL}; non-phase matched lossless systems exhibit oscillating P_{NL}; in lossless systems, P_{NL} peaks at short lengths. Also shown are example calculations of the near-degenerate four wave mixing conversion efficiency η **b** for lossless systems and **c** for lossy systems, showing a peak conversion at $L_{\mathrm{OPT}} = \ln(3) \cdot L_{\mathrm{att}}$. **b** and **c** are adapted with permission from Ref. [82]. Copyright (2016) American Chemical Society

nonlinear phase shift is given by [122]

$$\phi_{\mathrm{NL}}(t) = \frac{\gamma_R}{2\gamma_I} \ln\left(1 + 2\gamma_I P(t) L_{\mathrm{eff}}\right), \tag{10}$$

where $\gamma = \gamma_R + i\gamma_I$ can be calculated from Eq. (7), $L_{\mathrm{eff}} = L_{\mathrm{att}}[1 - \exp(-\alpha_0 L)]$ is the effective length, and $L_{\mathrm{att}} = 1/\alpha_0$. In the absence of loss, this reverts to the familiar form [80]

$$\phi_{\mathrm{NL}} = \gamma P L. \tag{11}$$

Equation (10) leads, for example, to the nonlinear generation of new frequencies via self-phase modulation through $\omega(t) = \omega_0 + d\phi_{\mathrm{NL}}(t)/dt$ [80]. The effectiveness of a nonlinear waveguide is commonly quantified by a figure of merit (FOM), chosen to compare the performance of different systems. A commonly used FOM is $\mathscr{F} = \gamma L_{\mathrm{att}}$ [123], which roughly computes the inverse power required to obtain one radian of phase shift over one attenuation length.

Note that Eq. (11) deceptively suggests that the nonlinear effects increase indefinitely with power; a more complete analysis should account for material damage effects at high powers. To illustrate this, Fig. 10a shows a schematic summary of the achievable nonlinear phase shift in a bulk material and a waveguide containing it. The blue curve shows an initial linear increase in the nonlinear phase shift with driving power following Eq. (11), reaching a maximum before material damage, associated with a maximum nonlinear index change $\Delta n_{\max}$. The red curve shows the equivalent effect in a nonlinear waveguide: the slope, given by γ, can be much larger than its bulk counterpart due to the omnidirectional field enhancements discussed. However, this is accompanied by a lower damage threshold. This effect is general, but particularly severe in plasmonic waveguides due to the potential presence of localized “hot spots” at the metal surface (see for example Fig. 5i). To account for this, Li et al. proposed

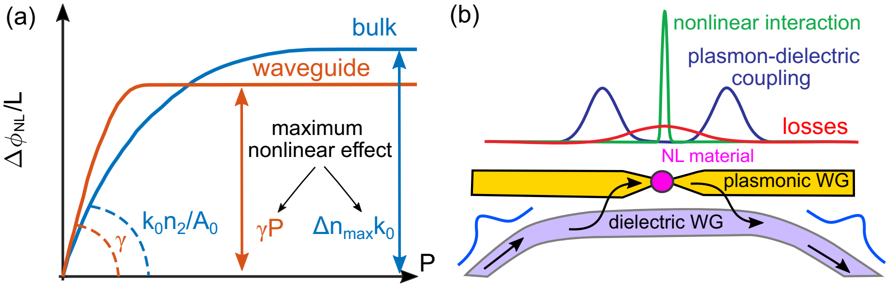

Fig. 10 **a** Schematic of the nonlinear phase shift per unit length $\Delta\phi_{\mathrm{NL}}/L$ versus driving power P for bulk material (blue), and for a waveguide (red). Both show an initial linear increase with slope $k_0 n_2/A_0$, and γ, respectively (A_0: beam area). Maximum nonlinear effects are limited by optical damage, associated with a maximum available refractive index change $\Delta n_{\max}$. Adapted with permission from Ref. [125]. Copyright (2018) American Chemical Society. **b** Nonlinear plasmonic circuits provide strong nonlinear interactions in small volumes, at the cost of propagation losses. In an optimized scheme, a dielectric waveguide strongly couples to a plasmonic WG, interacting with a nonlinear medium in a sub-wavelength mode and over approximately one attenuation length, before being coupled back into the dielectric waveguide. The light is coupled over an intermediate region (green), limiting losses to regions near the nonlinear medium (red) where nonlinear effects are strongest (green). Adapted with permission from Ref. [126], Copyright (2007) Springer Nature

the figure of merit [82]

$$\mathscr{F} = \gamma P_{0,th} L_{\mathrm{att}}, \tag{12}$$

where $P_{0,th}$ is the maximum power supported by the mode before damage occurs, and can be estimated from modal calculations of the electric fields around plasmonic hot-spots, combined with experimental measurements of material damage thresholds [124].

Once the above FOM is known, Li et al. showed that the maximum achievable nonlinear phase shift is given by $\Delta\Phi_{\mathrm{NL}}^{\max} = 2\mathscr{F}^2/3$, at an optimum device length $L_{\mathrm{OPT}} = \ln 3 \cdot L_{\mathrm{att}} \approx 1.1 L_{\mathrm{att}}$. For the specific case of nearly-degenerate four-wave mixing [127], this corresponds to a signal-to-idler conversion efficiency of $\eta = 4\mathscr{F}^2/27$. An illustrative full calculation comparing lossless and lossy waveguides, originally presented in Ref. [82], is shown in Fig. 9b, c. Subsequent work [125] proposed the concept "nonlinear effectiveness", which quantifies a mode's capacity to use a certain material's *maximum* nonlinearity: it was shown that this requires a strong electric *energy* confinement, and broadband slow light effects. A comprehensive comparison of several material and geometry combinations suggested that MDM structures perform best for compact efficient nonlinear optics [128].

We are now in a position to discuss typical recent experimental configurations for on-chip nonlinear plasmonics, illustrated in the Fig. 10b schematic: light from a linear dielectric waveguide is coupled into a subwavelength plasmonic region containing a highly nonlinear material. Here, the intense fields provide nonlinear optical effects over $\sim L_{\mathrm{att}}$, and the resulting nonlinear light is out-coupled into the dielectric waveguide. In such a way, low-power and low-footprint nonlinear effects are concentrated to a dedicated region, and losses are minimized. It is thus worthwhile reflecting on the requirements for achieving the large $\mathscr{F}$ in Eq. (12) in the context of plasmonic systems. Since L_{att} is typically of the order of a few wavelengths, one can compensate the small propagation loss with a large γ or using a higher power. However, the omnidirectional field enhancement producing a large γ for a certain $\chi^{(3)}$ lowers the damage threshold $P_{0,th}$. Moreso than for all-dielectric devices which can accumulate nonlinear effects using longer lengths, plasmonic nonlinear devices crucially require both a large $\chi^{(3)}$ and a high damage threshold. If used in hybrid structures, they should also posses a lower refractive index than the adjacent semiconductor, and ideally be compatible with industrially scalable fabrication. Recent experiments have shown compact nonlinear functions using commercially available polymers such as JRD1 [19] and MEH-PPV [127], (possessing a large $\chi^{(2)}$ and $\chi^{(3)}$, respectively), spin coated on a number of hybrid MDM waveguides on a silicon-on-insulator (SOI) platform (see also Sects. 4 and 5).

We note that an early theoretical analysis [129] came to the conclusion that nonlinear plasmonics was not well suited for applications requiring high conversion efficiency (e.g., all-optical switching and frequency conversion), since the maximum achievable nonlinear phase shift was calculated to be at most 0.1 rad, with nonlinear conversion efficiencies of order -30 dB, assuming that the maximum achievable index change was 1%. Applications which do not require high conversion efficiencies, such as nonlinear sensing and imaging which benefit from smaller mode volumes, were seen as more suitable. Recent developments in device designs have shown MDM plasmonic structures with -13 dB FWM conversion efficiency [130] over wavelength-scale propagation, and epsilon-near zero materials with nonlinear refractive index changes of 170% [118].

3.4 Material considerations

Due to the hybrid nature of nonlinear plasmonic waveguides, it is also important to consider how each constituent material contributes to the total γ. We may re-write Eq. (7) as $\gamma = \sum_m \gamma_m$, where γ_m is the contribution of a material m with nonlinear susceptibility $\chi_m^{(3)}$ to the total γ of a mode. The ratio $\gamma_m/\chi_m^{(3)}$ thus quantifies the degree of concentration of light to a particular medium for that mode. Figure 11a shows $\gamma_m/\chi_m^{(3)}$ for each material of the HPWG geometry considered in Fig. 4g as a function of the gap thickness t. Note that for large values of t, the larger ratio is in the underlying dielectric waveguide; for smaller t, the ratio is largest in the subwavelength spacer. Overall, the degree of concentration of light in the metal is always orders of magnitude less: this motivated early theoretical investigations to neglect the metal's contribution to the total nonlinear response in similar systems [116].

Calculating γ_m, i.e., each material's contribution to the total γ, shown in Fig. 11b, paints a different picture: since air has a $\chi^{(3)}$ that is seven orders of magnitude smaller than that of silicon [31], its contribution to γ is negligible. On the other hand, gold's $\chi^{(3)}$ is orders of magnitude larger, so that its contribution approaches that of silicon for smaller separations as the field overlap with gold increases. Overall however, silicon is the dominant contributor to the total γ for this particular HPWG configuration.

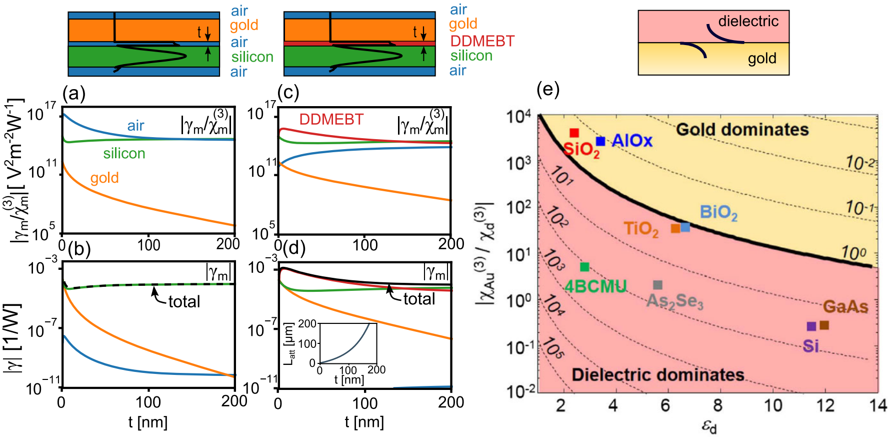

Fig. 11 **a** Calculated $|\gamma_m/\chi_m^{(3)}|$ and **b** $|\gamma_m|$ for each material m as labelled, in the case of the fundamental mode of a HPWG with an air spacer. For small t, the field is mainly confined in the air spacer, but silicon is the dominant contributor to γ. The associated attenuation length is shown in Fig. 4g. **c** Calculated $\gamma_m/\chi_m^{(3)}$ and **d** $|\gamma_m|$ for a HPWG with a DDMEBT spacer. The large field fraction in the spacer, combined with the large $\chi^{(3)}$ of DDMEBT, produces an enhanced overall γ. Inset in **d**: associated attenuation length. **e** Mapping of the nonlinear response for the SPP at a gold/dielectric (Au/d) interface assuming gold and different dielectrics as indicated. Contour plot of the figure of merit ρ as defined in Eq. (5) of Ref. [131], as a function of $\chi_{\mathrm{m}}^{(3)}/\chi_{\mathrm{d}}^{(3)}$ and ε_d. Adapted with permission from Ref. [131], Copyright The Optical Society. See Table 1 for material parameters used

Including a material with a large $\chi^{(3)}$ inside the spacer (e.g., DDMEBT [72]) can dramatically increase the total γ, as shown in Fig. 11c, d: for subwavelength t, the large field fraction in the spacer, in unison with its large $\chi^{(3)}$, dominates the contribution to the total γ, enhancing the performance of the underlying waveguide by at least an order of magnitude. Table 1 shows the linear and nonlinear parameters used. For equivalent calculations in 2D waveguides, see for example Ref. [91].

Beyond this illustrative example, the relative contributions to the total nonlinear response will depend on the materials' permittivities, susceptibilities, and geometric parameters. Such relationships were rigorously addressed by Baron et al. [131] for the simple case of a semi-infinite metal/dielectric SPP, where modes have an analytical form. To identify whether the metal- or the dielectric-contributions dominate, a figure of merit ρ was proposed and shown in Fig. 11e. Here, ρ depends on both the ratio of metal/dielectric permittivites, nonlinear susceptibilites, as well as intrinsic modal characteristics: $\rho < 0$ indicates that dielectric dominates the nonlinear response, whereas for $\rho > 0$ the gold dominates. Overall, low-index and low-susceptibility configurations (e.g., air, silica, and aluminum oxide) are metal-dominated; otherwise, the large fields at the metal surface enhance the dielectric's nonlinear response.

Table 1 Linear and nonlinear parameters of materials considered in simulations shown in Fig. 11, modified and expanded from Ref. [131] with additional materials that are relevant for hybrid plasmonics devices, such as the molecule DDMEBT, the polymer MEH-PPV, and monolayer (2D) MoS_2

Material	$n = \sqrt{\varepsilon}$	$\chi^{(3)}$ $m^2/V^2 \times 10^{-19}$	wavelength (μm)	References
Air	1.0006	1.7×10^{-6}	–	[31]
SiO_2	1.45	0.0025	1.3	[31,132]
Si	3.5	$1 + 0.3i$ (Fig. 11a)	1.55	[133]
		$25 + 0.0039i$ (Fig. 11b)		[134]
DDMEBT	1.8	2	1.5	[72]
MEH-PPV	1.65	$4.3 + 0.1i$	1.5	[127,135]
Au	$0.57 + 9.7i$	$800 + 250i$ (Fig. 11a)	1.55	[105]
		$4.67 + 3.03i$ (Fig. 11b)	0.8	[136]
Al_2O_3	1.8	0.0031	1.06	[137]
GaAs	3.5	$24 + 48i$	1.55	[138]
TiO_2	2.48	0.21	1.06	[31]
Bi_2O_3	2.5	0.24	1.5	[32]
As_2Se_3	2.4	$4.1 + 0.56i$	1.5	[32]
4BCMU	1.56	$-1.3 + 0.55i$	1.06	[31]
MoS_2 (2D)	5.0	2.4	1.0, 1.55	[139,140]

3.5 Other nonlinear effects

Harmonics generation

In the case of second- and third-harmonic generation, and non-degenerate four wave mixing, developing general analytic guidelines for optimal device length and maximum conversion efficiencies is more challenging. In such cases, designs are highly dependent on the mode overlap profiles and losses of the participating the pump- and harmonic-modes, which can be vastly different, and thus require analyses on a case-by-case basis. To quote a few examples, a theoretical study [141] of second-harmonic generation in a $\chi^{(2)}$-polymer plasmonic-nanoslot structure at 1550 nm predicted maximum conversion efficiency $\eta \sim 10^{-4}$ after propagating a length corresponding to the attenuation length ($\sim 20\,\mu$m). A HPWG using a $\chi^{(2)}$ material as the waveguide [142] or spacer [143] can yield a higher conversion efficiency (up to $\sim 8\%$), at the cost of a longer propagation length ($> 100\,\mu$m). Similar conclusions can be drawn from THG via $\chi^{(3)}$ effects [144].

Optical limiting and saturable absorption

In bulk media, the transmitted power is associated with $\Im m(n_2)$ as per Eq. (4); in waveguides, it is due to $\Im m(\gamma)$ as per Eq. (7) via Eq. (6). In lossless systems, $\Im m[\chi^{(3)}]$, $\Im m(n_2)$ and $\Im m(\gamma)$ all have the same sign. In plasmonic systems, which possess complex propagation constants, these quantities can have either a positive or nega-

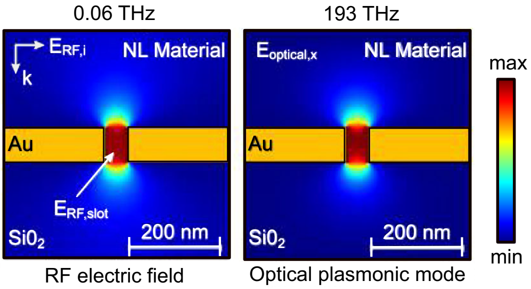

Fig. 12 Simulated two-dimensional electric field of the sub-THz field confinement (left) and optical plasmonic mode (right)containing a dielectric, showing high modal overlap and enhanced nonlinear interactions between frequencies that differ by five orders of magnitude. Adapted with permission from Ref. [150]. Copyright (2015) American Chemical Society

tive value, leading to a reduction- or increase-in the transmission at high intensities (i.e., optical limiting and saturable absorption (SA), respectively). Although nonlinear absorption is commonly seen as a limiting factor to nonlinear optical devices [122], it can be harnessed in nonlinear plasmonic devices in the context of "active plasmonics" [145], whereby changes in the absorption properties close to the metal/dielectric interface, driven by an external signal, can modulate the plasmonic mode, most recently shown to provide a means of providing low-power all-optical switching by integrating graphene on a MDM slot [146]. Nonlinear absorption effects in metals are strongly dependent on the pulse duration of the incoming light, even at constant wavelength. This pulse-length dependent absorption has been measured in detail for gold [147], and is due to the complex electron dynamics induced by an incoming optical pulse, although this effect is weaker away from the interband region in the near-infrared [148]—see Ref. [102] and Ref. [149] for related experimental and theoretical reviews.

The Pockels effect

We have so far considered the Kerr nonlinearity—whereby changes in the refractive index are proportional to quadratic fields (i.e., the intensity)—as a representative degenerate case when considering nonlinear plasmonics in chip-compatible structures. The above discussion, and much of the underlying physics, can be extended to *linear* electro-optics (EO) effects, i.e., the Pockels effect, whereby changes in the refractive index are proportional to linear fields via $\chi^{(2)}$. Most notably, a metal nano-slot containing a $\chi^{(2)}$ medium leads to a strong nano-scale Pockels effects via large modal overlap between the short-wavelength optical fields E_{OF} and long-wavelength fields E_{RF}, as shown in Fig. 12 [150]. As a result, such fields efficiently interact via the underlying nonlinear medium: the propagation constant of the optical field changes via $\Delta n_{\mathrm{eff}} \propto \int \chi^{(2)} E_{\mathrm{RF}} E_{\mathrm{OF}^2} dxdy$ [151]—while this mode overlap is small in dielectric waveguides, it can be large in plasmonic structures, leading to more compact electro-optic devices operating at low powers [152,153]. Here the effective index change of the optical mode is given by [151]

$$\Delta\beta = k_0 \Delta n_{\mathrm{eff}} = \frac{1}{2} n_0^2 r_{33} \Gamma n_{\mathrm{s}} E, \tag{13}$$

where r_{33} is the electro-optic coefficient [31], and where Γ and n_s are a optical mode-dependent field-power interaction factor and a slow-down factor, respectively, defined in Ref. [151]. Equation (13) assumes that the dominant nonlinear effects occur in the slot, in a non-perturbative regime, and neglects losses, but it demonstrates how nonlinear plasmonics effects are enhanced via the same physical mechanisms underpinning the heuristic formula of Eq. (8). The most commonly used electro-optic material is $LiNbO_3$ [101], and organic electro-optic (OEO) materials have recently been developed and included in dielectric-plasmonic devices [19], for field sensing at GHz and THz frequencies [150] and electro-optic data modulation with extremely low footprints (~ 2.4 Tb/s/mm^2 [154]).

4 Nonlinear experiments with plasmonic waveguides

With the widespread use of commercially available numerical solvers (e.g., finite element, finite-difference time domain, and beam propagation techniques, to name a few), plasmonic waveguide structures have been the focus of a large number of numerical studies. Many nonlinear plasmonics experiments consider planar substrates containing metal nanostructured arrays [53], whose linearly and nonlinearly coupled modes are typically excited through external, diffraction limited illumination. The waveguide-equivalent version of such structures often rely on placing such nano-antennas on top of [59,155] or at the endface of [156] a waveguide. More efficient nano-coupling requires careful design [69,157], and such structures often require multiple fabrication steps that demand nanometre-precision alignment [55]. Early nonlinear plasmonic waveguides tended to relatively weak nonlinear responses and, being a few wavelengths long, characterizing them was challenging, often requiring sensitive measurements [158]. We now provide an introductory overview of nonlinear experiments in plasmonic waveguides. We first consider wave-guiding structures formed by a single metal/dielectric interfaces to achieve their nonlinear function, before moving to hybrid systems. The nonlinear effects considered are due to guided surface plasmons that are compatible with photonic circuitry, although most experiments rely on free-space excitation.

4.1 Surface plasmon polaritons

The pioneering experimental work on nonlinear plasmonics can be traced back to the 1970s with the first observation of second harmonic generation by exciting SPPs on a bulk silver film [159], measuring more than an order-of-magnitude enhancement in SHG emerging from propagating plasmon excitation, when compared to front-surface reflection. Later fundamental studies used a wavevector-space spectroscopy technique to observe this process in more detail [160], directly measuring the annihilation of two surface plasmons and creation of second-harmonic photons.

The first device-driven nonlinear plasmonics experiments targeted nonlinear switching: in first instance, this can be achieved by inducing nonlinear changes in the dielectric permittivity ε_m at the metal's surface, which alters the propagation constant in Eq. (5) and thus modulates SPP excitation on the time scales of the material's

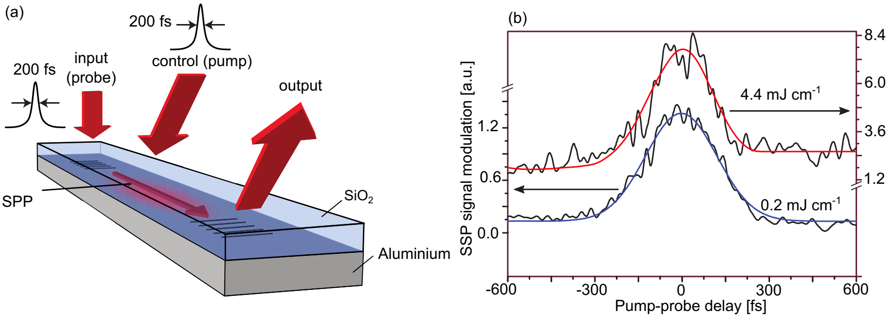

Fig. 13 "Active plasmoncs" experiment summary. **a** Schematic illustrating a signal beam exciting and collecting SPPs at an aluminium–silica interface via gratings. **b** The change in the SPP coupling properties and the induced absorption contribute to modulating the transmitted signal at ∼ 200 fs timescales. Adapted with permission from Ref. [145], Copyright (2009) Springer Nature

response. Early experiments with metal/semiconductor waveguides used aluminium grating structures adjacent to silicon, and showed high-contrast switching operation [161], but operated near silicon's absorption edge at $\lambda = 1.064\,\mu\text{m}$, where the response is dominated by free-carrier generation and lattice heating, which is in the nanosecond to millisecond range.

Ultrafast nonlinear modulation enabled by plasmonics started emerging from the mid-2000s. In one notable experiment [145], summarized in Fig. 13, the transmission of ultrafast surface plasmon polariton pulses propagating on an aluminium/silica interface could be modulated by an external probe, with response times of ∼ 200 fs. This was enabled by operating at the absorption peak of aluminium ($\lambda = 780\,\text{nm}$), where changes in the real- and imaginary-parts of its permittivity were due to ultrafast interband transitions. In particular, these were due to nonlinear changes at the metal surface, and occurred only for a polarization parallel to the propagation direction; a slower, thermally-driven polarization-independent response was also identified.

Rich nonlinear electron dynamics at metal surfaces can also lead to the external excitation of surface plasmon polaritons directly on a gold film—typically disallowed due to lack of phase-matching between plasmonic- and free-space beams—via the formation of an effective "nonlinear grating" [162]. Nonlinear plasmonic modulation can alternatively be addressed via nonlinear changes in the permittivity of the adjacent dielectric: typically, gold/silicon bulk SPPs [163] and gold/polymer waveguide SPPs [164] enable modulation speeds of 0.1–1 ms.

Related studies explored plasmonic coupling due to the nonlinear interactions between modes of different harmonics in plasmonic films. Palomba et al. experimentally demonstrated the nonlinear excitation of surface plasmons at $\lambda = 613\,\text{nm}$ via four-wave mixing of ultrashort infrared in a Kretschmann configuration [165]. These fundamental results, which highlight the potential for nonlinear manipulation of surface plasmons, highlighted how important surface effects are: despite the fact that gold possesses a bulk $\chi^{(3)}$, the surface $\chi^{(3)}$ at the gold/dielectric interface was the dominant nonlinear source. Subsequent experiments on the same structure measured three distinct four-wave mixing effects, including nonlinear reflection off the gold

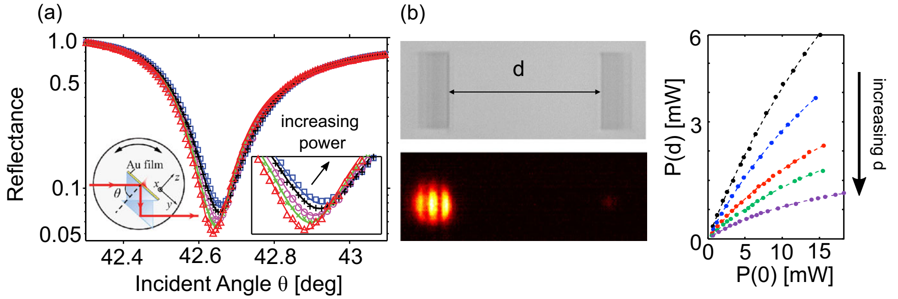

Fig. 14 Nonlinear absorption measurements in SPP waveguides. **a** Kretschmann measurement: reflectance as a function of incident angle θ. For increasing power levels, the dip shifts and its minimum increases. Inset: Zoom-in of the Kretschmann dip, and experimental setup. Adapted with permission from Ref. [136] (Copyright The Optical Society). **b** Grating coupling measurement. Top left: Micrograph of a SPP waveguide (d $= 40\,\mu$m) and its grating couplers. Bottom left: the same waveguide illuminated by a laser spot on the left grating, showing transmission on the right grating. Right: measured average power transmitted by the SPP as a function of input power for varying waveguide lengths d, showing optical limiting. Adapted with permission from Ref. [169], Copyright (2015) by the American Physical Society

surface, the excitation of evanescent fields, as well as the excitation of the nonlinear surface plasmon [166]. The nonlinear conversion was later improved by nanostructuring the gold surfaces, where local field enhancements improved the conversion efficiency with respect to a smooth film by a factor of ~ 25 [167]–2000 [168] times. These pioneering studies showed novel chip-compatible excitation mechanisms as a result of the large nonlinearities at gold surfaces, driven by large local intensities.

A series of subsequent experiments investigated the intrinsic $\chi^{(3)}$ of gold by probing the nonlinear "self-action" effects of SPPs, whereby a SPP modifies its own propagation characteristics. De Leon et al. [136] investigated intensity-dependent SPP propagation on a gold film, and used it to obtain the complex $\chi^{(3)}$ experimentally (this is challenging, and most experiments estimate its magnitude [102]). The authors measured a power-dependent reflection spectra of the Kretschmann configuration as shown in Fig. 14a; a nonlinear transfer matrix model was then used to obtain $\chi^{(3)} = 4.67 \times i3.03$ as a single fitting parameter at $\lambda = 800$ nm. A review by the same authors [102] found that measured values of $\chi^{(3)}$ of gold can vary by several orders of magnitude, depending on wavelength, pulse duration, or the nature of the nonlinear experiment. Most strikingly, similar measurements of the nonlinear absorption of SPPs at gold/air interfaces [169] resulted in $\chi^{(3)}$ values which were three orders of magnitude larger. In this case, the authors excited SPPs on a gold film using asymmetric gratings, which also collected the light, as shown in Fig. 14b(left). $\chi^{(3)}$ was then deduced from systematic optical limiting measurements, also in Fig. 14b(right). The authors attributed the apparent $\chi^{(3)}$ discrepancy to potential differences in the structure's surface roughness. These examples also serve to illustrate the difficulties in obtaining reliable and consistent nonlinear parameters for metals.

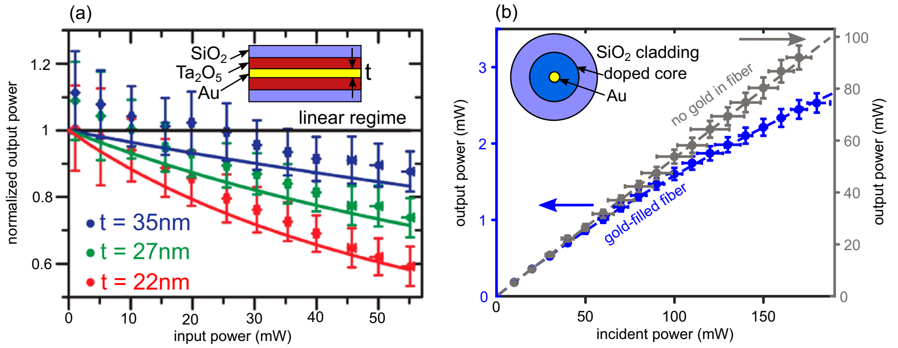

Fig. 15 **a** Nonlinear transmission for the LR-SPP transmitted by 3 mm-long thin-film plasmonic waveguides using 200 fs pulses and $\lambda = 1030$ nm, using gold thicknesses of $t = 35$ nm (blue), $t = 27$ nm (blue), $t = 22$ nm (blue). Larger relative nonlinear absorption was measured for thinner films. Adapted with permission from Ref. [106]. Copyright (2016) American Chemical Society. **b** Nonlinear transmission for the LR-SPP transmitted by a 1 cm-long gold nanowire plasmonic waveguide (gold diameter: 100 nm), integrated within the core of a step index fiber (inset schematic), using 30 fs pulses and $\lambda = 1560$ nm. Optical limiting (blue) is observed compared with the equivalent optical fiber with no gold wire in its core (grey). Adapted with permission from Ref. [170], Copyright (2018) by the American Physical Society

4.2 Long-range surface plasmon polaritons

In the 1980's, the first SHG experiments on nonlinear LR-SPPs were reported, which sought to observe some of the emerging theoretical predictions [171], and first investigated the trade-off between confinement and propagating distance. For example, in 1983 Quail et al. [172] showed that the field excitation on both surfaces of the film leads to a two-order of magnitude improvement in harmonic generation compared to an equivalent bulk film.

Experiments targeting the $\chi^{(3)}$ response of gold via nonlinear absorption of LR-SPPs on both thin metal films [106,173] and metal nanowires [170] were recently performed. In this case, nonlinear effects were measured after mm- and cm-scale propagation distances. Lysenko et al. measured nonlinear absorption of plasmonic modes in waveguides formed by gold nanofilms of different thickness (22-35 nm) surrounded by bulk SiO_2 and Ta_2O_5 nanolayers. The authors measured a thickness-dependent nonlinear absorption induced by 200 fs pulses at 1064 nm (Fig. 15a), and developed a nonlinear wave equation that generalizes Eq. (6) to include gold's temporal response, which accounted for non-instantaneous contributions from free electrons. Their model indicated that $\chi^{(3)}$ nearly doubles as the film thickness is halved. The authors suggested that these changes in $\chi^{(3)}$ are due to increased collisions of electrons in thin gold layers. Such quantum size effects are significant for thinner metal layers: for example, Qian et al. [174] showed more than a radian nonlinear phase shift for a bulk 3 nm gold film under similar conditions.

Tuniz et al. observed nonlinear absorption of long-range plasmons on gold nanowires (diameter: 100 nm) integrated within the core of a step-index silica fiber [170], after centimetre-scale propagation. The integration of sub-micron metal wires in fibers [175] typically leads to wire break-up; the authors overcame this limita-

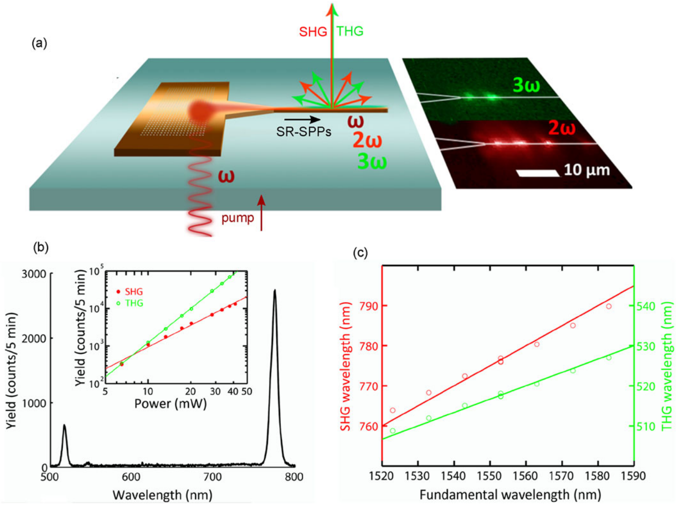

Fig. 16 Second- and third-harmonic generation on single Au nanowires. **a** Schematic representation of the experiment: a hole array is illuminated TM-polarized femtosecond pulses, ($\lambda = 1550\,\mathrm{nm}$). SPPs are adiabatically converted to SR-SPPs by reducing the width of the wire. Visible light, corresponding to harmonics-generation, is scattered from the wire. **b** Typical measured spectrum showing peaks at 775 nm (SHG) and 517 nm (THG). Inset: solid line power fits to the measured yield as function of power. The slopes of 2 (red), and 3 (green) respectively confirm the required power dependence for SHG and THG. **c** Wavelength dependent SHG and THG. Adapted with permission from Ref. [176]. Copyright (2016) American Chemical Society

tion by including the gold nanowire in the core of a single mode optical fiber, which allowed to access a unique regime where the plasmonic mode was the only effectively propagating mode, which directly interfaced with a single mode fiber. In the regions where the wire breaks up, light was recaptured by the fiber, and then re-coupled into the plasmonic mode at the subsequent wire junction. This approach solved the problem of detrimental wire discontinuities and fabrication imperfections along the gold nanowires, by preventing the light from scattering away, and enabled measurements of ultrafast nonlinear absorption (30fs pulse duration, 1560 nm wavelength). Self-phase modulation effects, on the other hand, were dominated by the silica matrix. The nonlinear absorption coefficient obtained was in agreement with expectations from experimental trends [102].

4.3 Short-range surface plasmon polaritons

Experimental observations of nonlinear effects on propagating short-range surface plasmon polaritons are uncommon, due to the short attenuation lengths (typically, of the order of a few μm), and due to challenges in efficiently coupling to such nanoscale modes [69]. In 2016 De Hoogh et al. [176] were the first to report nanoscale nonlinear optics with propagating plasmonic modes on a photonic chip. They showed both second- and third-harmonic generation due to surface- and bulk-nonlinearities on single gold nanowires. The short-range SPP modes were excited using a previously reported adiabatic taper approach [177] shown in the schematic of Fig. 16a. The authors conclude that the measured THG and SHG, shown in Fig. 16b, c, emerge both from the local enhancement induced by plasmonic nano-focusing before being launched into the nanowire, and from the modes propagating on the nanowires themselves. Note that although the pump- and harmonic-modes are not phase matched, this did not preclude higher harmonic generation in this lossy system. More recently, Chen et al. [178] showed that a coupled plasmonic *two*-wire system—formed by two 6 μm-long 100 nm gold nanowires, separated by 100 nm—can selectively generate both symmetric- and anti-symmetric second-harmonic modes by judicious mixtures of the 1560 nm pump modes, tailored via the input coupling conditions. This approach might find use in providing additional degrees of freedom for nonlinear circuit designs, such polarization control, waveform shaping, and selective routing.

4.4 Nanofocused surface plasmon polaritons

The appeal of plasmonics-based approaches is the ability to guide and then concentrate light to deep subwavelength volumes, which can be achieved by tapering a waveguide to the nanoscale, as shown in Fig. 3. In this case, the short-range plasmons concentrate light in all directions, potentially within mode areas of less than $(\lambda/100)^2$, and the region in this case, the region in close proximity to the sharp tip of the tapered plasmonic strucures gives rise to the field enhancements that further favour nonlinear processes compared to the bulk (non-tapered) case. This approach has been shown to enhance nonlinear processes inside the metal and in the surrounding dielectric region, with applications in nonlinear imaging and nonlinear light generation.

In one experiment, Verhagen et al. [177] experimentally showed the enhancement of nonlinear multi-photon processes associated with energy levels of Erbium, which surrounded a tapered silver plasmonic waveguide pumped at 1.49 μm. The measured far-field intensity enhancement due to this nonlinear process provided evidence of local near-field enhancements, which would otherwise be difficult to observe without using near-field techniques. Other experiments have utilized the intensity enhancements inside a hollow metal cantilever taper—as shown in Fig. 17**a**—to produce high-frequency harmonics. Despite the fact that small apertures formed by perfect conductors cut off and do not support propagating modes, Park et al. [179] harnessed a peak increase in the field intensity near a taper's aperture, shown in Fig. 17b, as a result of a subtle interaction between the incoming field, and the forward- and backward-propagating surface plasmons. The local field was enhanced by a factor of up to 350, which the authors use to produce up to 43 harmonics of Xenon gas, into the extreme ultraviolet (UV), pumping with near-infrared (NIR) radiation. The experimental results showcasing these results are plotted in Fig. 17c.

Other approaches use the metal itself as the nonlinear medium, driving the nonlinear processes upon tapering of the metal waveguide. Having previously demonstrated the ability to guide arbitrary femtosecond short-range plasmons pulse to a plasmonic nanofocus (directly revealed by SHG-assisted interferometric cross-correlation measurements [181]) Raschke and collaborators [180] used four-wave mixing effects for nonlinear imaging (apex radius: 15 nm). The measured conversion efficiency was 10^{-5},

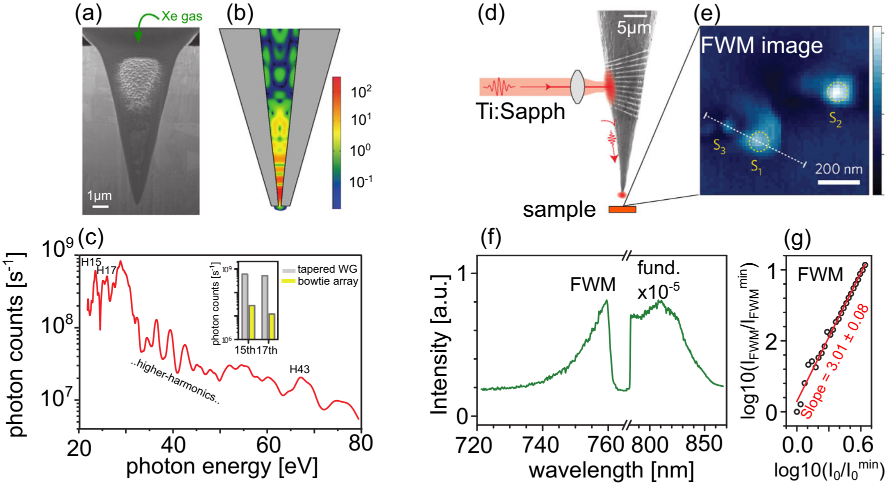

Fig. 17 Examples of nonlinear enhancement with guided plasmonic nanofocusing. **a** Cross-sectional view of a tapered metallic waveguide, filled with Xe gas. **b** Calculations showing the intensity ($\lambda = 800$ nm) inside the waveguide as it propagates down the tip, producing an enhancement close to the aperture output. **c** Measured UV spectrum spanning from the 15th (H15) to 43rd (H43) harmonic of the input. Inset: comparison with a bowtie antenna array, showing improved conversion efficiency. Adapted with permission from Ref. [179], Copyright (2011) Springer Nature. **d** Experiment schematic of nonlinear FWM of nanofocused SPPs. 10 fs pulses are launched into a grating coupler. The resulting SPPs focus onto a nano-tapered Au tip that is 5 nm away from a sample to be imaged via nonlinear nanomicroscopy. **e** Near-field FWM image of a Si–Au step, showing plasmonic hotspots. **f** Example measured FWM ($\lambda < 760$ nm) and fundamental SPP ($\lambda > 785$ nm) at the tip. **g** Power dependence of spectrally integrated FWM signal on a log–log scale, showing a slope of ~ 3. Adapted with permission from Ref. [180], Copyright (2011) Springer Nature

which was enough to observe the plasmonic hot-spot dynamics of a separate gold surface with 50 nm resolution. A number of different experiments on the same geometry revealed several intriguing nanoscale nonlinear effects, including electron emission from the tip [182], and a nanostructure-induced enhancement of $\chi^{(3)}$ of gold for sharper metal tips via longitudinal field gradients [183]. These results highlight the many opportunities provided by guided-wave nonlinear plasmonics due to localized strong field effects, even in the face of low nonlinear conversion efficiencies. We refer the reader to Ref. [184] for a recent and comprehensive review of strong-field nonlinear nano-optics.

4.5 Hybrid plasmonic waveguides

While the nonlinear plasmonic experiments presented so far relate to guided-wave structures, they are one step away from being compatible with photonic integrated circuits, where they would interface with dielectric waveguides [43,57,58,186,187]. Sederberg et al. [185] bridged silicon photonics [3] with nonlinear plasmonics, reporting optical third harmonic generation enhanced by plasmonics on a silicon nanowire, as summarized in Fig. 18a. In this experiment, a gold film was deposited on top of a silicon waveguide, shown in the scanning electron microscope (SEM) image of

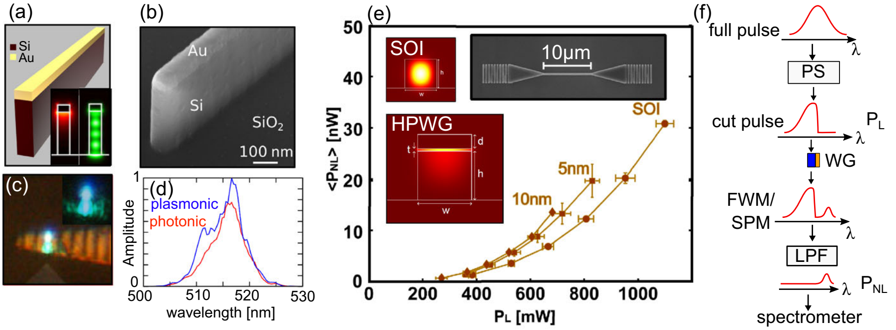

Fig. 18 **a** Schematic silicon/gold nanoplasmonic waveguide. Inset: calculated intensity of its fundamental (left) and third-harmonic (right) modes. **b** SEM of the fabricated silicon plasmonic waveguide. **c** Optical microscope image of visible light emission from the nanoplasmonic waveguides due to third harmonic generation. **d** Comparison of the third-harmonic spectrum obtained for a bare- and plasmonic-Si waveguide for the same incident power, showing plasmonic enhancement of $\sim 30\%$. Adapted with permission from Ref. [185], Copyright (2015) by the American Physical Society. **e** FWM power P_{NL} transmitted by a HPWG for varying input power P_{L} and spacer gap thickness as labelled, compared with a bare SOI waveguide. Insets show SOI and HPWG mode calculations, and a SEM image of one of the waveguides. Adapted with permission from Ref. [158], Copyright The Optical Society. **e** Schematic of the associated measurement approach [148]: a pulse is cut using a pulse shaper (PS) and coupled into a WG. The resulting spectral broadening is spectrally filtered using a long pass filter (LPF), and P_{NL} is detected using a spectrometer

Fig. 18b. Light was launched and collected via end-fire coupling, with NIR pulses ($\lambda = 1.55\,\mu$m) driving third-harmonic generation ($\lambda = 517$ nm) in a waveguide of length $5\,\mu$m, as shown in Fig. 18c. Note the significant experimental challenges associated with this measurement: the short attenuation length of silicon at visible frequencies ($L_{\mathrm{att}} \sim 600$ nm) makes phase-matching unnecessary (see Fig. 9a). Compared with a bare silicon waveguide, the THG signal from the plasmonic-enhanced waveguide was approximately 27% stronger (as shown in Fig. 18d) in a device that was three times shorter, resulting in a maximum conversion efficiency of 2.3×10^{-5}.

More recently, the high confinement and low losses of HPWGs were exploited for compact SHG and sum frequency generation (SFG). One experiment [188] measured a SHG conversion efficiency in a HPWG waveguide formed by CdSe (length: $5\,\mu$m; width: 360 nm) deposited on a gold film, separated by a 10 nm Al_2O_3 spacer, and pumped at 800 nm [188]. In this case, the dominant nonlinear effect originated from the CdSe, and was enhanced by the excited HPWG modes. The authors selectively coupled to the photonic- and plasmonic-modes of this multi-mode system: the latter showed a 20-fold SHG enhancement with respect to the former, with a maximum conversion efficiency of $4 \times 10^{-5}\,\mathrm{W}^{-1}$, and with several prospects for further improvement (e.g., higher quality gold/silver films, better nonlinear mode overlaps, and by optimizing nanowire cavity effects.) In this particular experiment, phase matching also did not play a role due to the large loss of the second harmonic mode. A subsequent experiment on an AlGaInP-based HPWG structures [189] directly measured the evolution of second-harmonic- and sum-frequency-generation (SFG) in phase-matched $\sim 15\,\mu$m length waveguides and $\sim 1\,\mu$m HPWG microresonator disks, with peak SHG conversion efficiencies up to 2.6×10^{-6} . A comparison with all-dielectric waveguides showed more than a 1000-times enhancement, and the efficiencies per unit length were claimed to be competitive with state-of-the-art lithium niobate devices. Most notably, a broadband SFG processes—wherein multiple combinations of phase-matched nonlinear frequencies could be addressed via a supercontinuum source—were three to five times more efficient than SHG as a result of the lower losses of the modes involved.

Measuring Kerr nonlinearities in comparable micrometre-length waveguides is more challenging, since the phase shifts can be as low as $\sim 10^{-4}$ rad [91], resulting in negligible spectral broadening due to self-phase modulation. Nevertheless, measuring such effects can be important for benchmarking the performance of plasmonically-enhanced HPWGs. To address this requirement, Diaz et al. [158] presented a method to sensitively measure self-phase modulation in micro-scale waveguides. The experimental procedure relies on shaping each pulse via an all-reflective waveshaper, such that long wavelength are completely removed, leading to a sharp spectral edge. Such spectrally cut pulses are then coupled to the waveguide, where the small nonlinear signals generated in the cut region can be detected after removing the pump light with a spectral filter. This background free measurement enables sensitive measurements of Kerr nonlinear effects. A comparison between a silicon waveguide and a hybrid plasmonic waveguide with a silicon nitride spacer, shown in Fig. 18e, reveal no significant improvement, since the $\chi^{(3)}$ of silicon nitride is too low to boost γ above that of the bare silicon waveguide, despite the sub-wavelength mode area. A later theoretical analysis [91] revealed that DDMEBT in HPWG can enhance the SOI γ by an order of magnitude (see also Fig. 11d).

Finally, we highlight a recent experiment which revealed self-focusing effects in a hybrid gold/silica/chalcogenide structure at telecommunication wavelengths over distances of $\sim 100\,\mu$m, harnessing the field enhancements and the large nonlinearities in chalcogenide [190].

In spite of the early promise of hybrid plasmonic waveguides for nonlinear applications [191], and their potential to enhance the performance of the underlying dielectric waveguide [91], HPWGs have enjoyed limited use in PICs, perhaps because the associated fabrication/design difficulties to be overcome are too large, and the expected performance improvement too little. A number of recent experiments provide compelling evidence that metal-dielectric-metal waveguides [83] are easier to fabricate, can be immediately interfaced with dielectric waveguides, and provide giant nonlinear effects after wavelength-scale guidance. We now discuss nonlinear MDM waveguides, starting with their Kerr nonlinear performance. Additional circuit-integrated MDM nonlinear effects are discussed in Sect. 5.

4.6 Kerr plasmonic slot waveguides

Early nonlinear experiments with MDM waveguides showed evidence of all-optical switching in plasmonic directional couplers [192] formed by adjacent 80 nm wide plasmonic slots that were a only a few micrometres long [193], operating at 1550 nm. Despite the low footprint, these switches were reliant on the metal nonlinearity, were prone to optical damage, and required 5 kW of peak power.

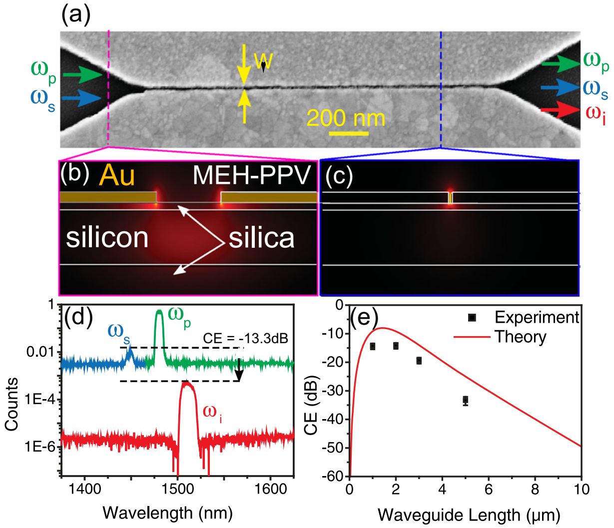

Fig. 19 **a** SEM image of a gap plasmon waveguide on a SOI substrate, of length L = 2 μm and gap width $w = 25$ nm. Arrows indicate a schematic of the FWM experiment, whereby a pump at frequency ω_p (green) and a signal at ω_s (blue) generate an idler at ω_i (red). **b** Mode intensity calculations at the input taper region and **c** in the plasmonic slot region (right), used for coupling via an adiabatic transition. **d** Example pump/signal spectrum and generated idler spectrum, showing -13 dB conversion signal-to-idler conversion. **e** Conversion efficiency versus waveguide length for different lengths of the waveguide (black markers), compared with theory (red line)—see also Fig. 9c. From Ref. [127]. Reprinted with permission from AAAS

More recent approaches have relied on incorporating high-index dielectrics inside the plasmonic slots. The highly nonlinear plasmonic modes are accessed from dielectric waveguides via efficient modal conversion schemes, e.g., by placing the plasmonic slot either on top of [127] or adjacent to [194] the waveguide, most commonly with a tapered section to assist the mode transformation [195,196]. Compared to the HPWG shown in Fig. 5g, the plasmonic slot geometry enables evaporation or spin-coating of a highly nonlinear material as a very last fabrication step. Nielsen et al. [127] used this approach to report giant four-wave mixing (FWM) conversion efficiencies in a plasmonic slot waveguide of 2 μm in length. The waveguide is shown in Fig. 19a, and consists of the commercially available, highly nonlinear polymer MEH-PPV, which is sandwiched in a gold nano-slot (gap width: 25 nm). Light was coupled into the waveguide and collected via gratings and tapers, and the entire device was on a silicon-on-insulator substrate covered by a thin silica spacer (total device length: 25 μm). The FWM process was attributed to the plasmonic slot mode profile: Fig. 19c, since the γ of the modes guided by all other plasmonic elements—such as the taper region shown in Fig. 19b—was negligible. The authors measured a maximum signal-to-idler conversion efficiency of −13.3 dB, (i.e., 4.7%), as shown in Fig. 19d, and longer device lengths led to a decrease in the conversion efficiency as shown in Fig. 19e, in agreement with theoretical predictions.

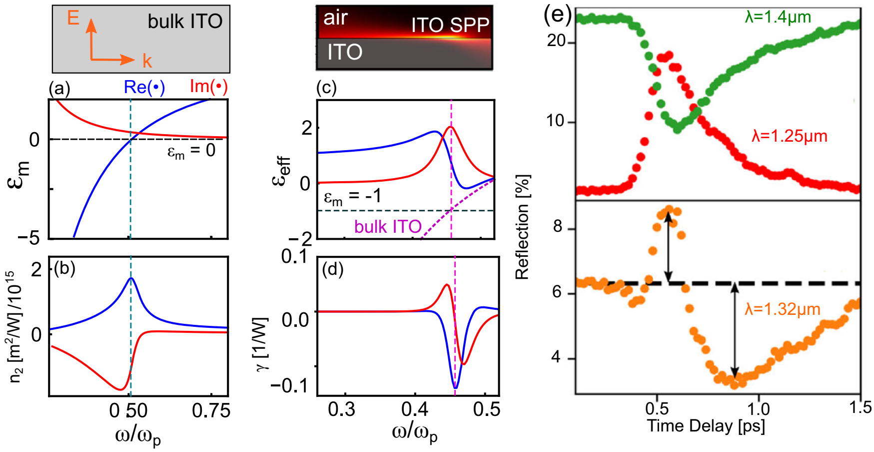

Fig. 20 Linear and nonlinear properties of bulk ITO and ITO SPPs [77]. **a** Real (blue) and imaginary (red) parts of ITO's relative permittivity $\varepsilon_m(\omega) = \varepsilon_\infty - \omega_p^2/(\omega^2 + i\Gamma\omega)$, $\varepsilon_\infty = 3.8055$, $\omega_p = 2\pi \times 473$ THz, and $\Gamma = 2\pi \times 22$ THz [118]. **b** Real (blue) and imaginary (red) parts of ITO's n_2 according to Eq. (4) taking constant $\chi^{(3)} = (1.6 + 0.5i) \times 10^{-18}$ m^2/V^2, showing a maximum when $\Re e(\varepsilon_m) = 0$ (i.e., at $\omega/\omega_p = 0.51$). **c** Real- and imaginary-parts of $\varepsilon_{\text{eff}} = n_{\text{eff}}^2$ of the ITO/air SPP mode from Eq. (1) (blue- and red-lines, respectively). Dashed magenta line: $\Re e(\varepsilon_m)$. **d** Real- and imaginary-parts of γ. Maximum $|\gamma|$ occurs when $\varepsilon_m = -1$ (i.e., at $\omega/\omega_p = 0.46$). **e** Experimentally measured nonlinear reflectance of ITO SPP pump-probe experiments. Labels indicate the different probe wavelengths considered, near the ENZ wavelength (here: $\lambda_{\text{ENZ}} = 1.235$ nm). Adapted from Ref. [200] under a creative commons license (CC BY 4.0)

4.7 Plasmonic waveguides with epsilon-near-zero materials

Before moving to the next section, we briefly discuss a recent development in nonlinear plasmonics that has attracted much attention, namely the realization that bulk materials possessing a real part of the permittivity $\varepsilon = \sqrt{n_0}$ that is close to zero (i.e., "epsilon-near-zero" (ENZ) materials) have an extremely large Kerr nonlinearity [197]. At first glance, when $\Re e(n_0) \to 0$ in Eq. (4), n_2 diverges—in fact, this is an artefact of the perturbative approach that was used to derive it [31]. In this case, changes in the intensity-dependent refractive index are more accurately described directly by [112]

$$n = \sqrt{\varepsilon + 3\chi^{(3)}|E|^2}. \tag{14}$$

Experimentally, ENZ materials have been show to yield extraordinarily large refractive index changes of 170% in Indium Tin Oxide (ITO) [118], and similar effects were measured in Aluminium-Doped Zinc Oxide (AZO) [198], and artificial metamaterials [199]—see for example Ref. [197] for a recent review of ENZ media. Figure 20a shows the relative electric permittivity of ITO, and Fig. 20b shows the associated n_2 according to Eq. (4), with the largest n_2 occurring where $\Re e(\varepsilon_m) = 0$.

But how to to harness ENZ materials for *guided-wave* devices with extreme nonlinearities? Reported approaches include operating a waveguide containing an ENZ material at the frequency where $\varepsilon_m = 0$ [201–204], or operating the waveguide with effective mode permittivity near cutoff such that $\Re e(\varepsilon_{\text{eff}}) = \Re e(n^2_{\text{eff}}) = 0$ [205–207]. Further insight can be obtained by noting that, according to Eq. (14), large nonlinear changes in n can also be driven by large $|E|^2$. This is the case for bulk ENZ media [77]: the transverse field has a local maximum at the ENZ wavelength, since it corresponds to a local minimum in the group velocity [77]. Furthermore, the longitudinal field can be further enhanced for TM polarization at angled incidence [118] due to the continuity of the normal component of the displacement field [197].

For waveguides formed by ENZ media, evaluating the nonlinear response requires calculating the nonlinear coefficient γ via Eq. (7), although insights can also be obtained from the factorization of Eq. (8). It is valuable to consider the simple case of a bulk SPP propagating at an air/ITO interface: Fig. 20c shows its real- and imaginary-parts as a function of frequency, and Fig. 20d shows the calculated associated γ according to Eq. (7). In contrast to the bulk case, the largest Kerr nonlinearities here occur at frequencies near $\varepsilon_m = -1$, which is the point of the lossless electrostatic surface plasmon polariton [41]. A recent study also computed the associated v_g and effective modal area, showing that these two parameters are indeed simultaneously minimized near this electrostatic plasmon resonance condition [77]. Similar calculations on other plasmonic waveguides led to the same conclusion. One key message of this analysis was that the enhanced Kerr nonlinearity in both bulk ENZ media and guided-wave structures can be understood in this unified framework of omnidirectional field enhancement.

In all cases, the associated losses are quite large, even by plasmonic standards: the calculated attenuation lengths for ITO nanowires/nano-apertures are of the order of 50–100 nm, suggesting that, rather than wavelength-scale waveguides, sub-wavelength-thickness metasurface arrays (e.g., pillars and nanoholes) are most appropriate for boosting Kerr nonlinear responses of ENZ media. A number of experiments have been performed on similar planar ENZ metamaterials [199] and metasurfaces [119], extending the available wavelengths where giant optical nonlinearities can be harnessed. In the present context of guided-wave structures, ultrafast all-optical switching was most recently measured using bulk ITO surface plasmons near the ENZ wavelength using a Kretschmann configuration [200], as shown in Fig. 20e. Analogous experiments in thin films showed third harmonic generation enhancements [208]. Such materials and geometries are compatible with CMOS fabrication technologies. Given these promising results, future studies will undoubtedly elucidate the subtle and counter-intuitive physics underlying the large nonlinearities of ENZ materials, clarifying their feasibility as mass-producible components for chip-compatible sub-wavelength nonlinear devices.

5 Nonlinear plasmonic circuits

The structures in Sect. 4 show the impressive potential of guided-wave nonlinear plasmonic applications of individual, self-standing devices. Integrating or post-processing similar nonlinear plasmonic structures on readily available off-the-shelf dielectric waveguides has the power to grant them with additional, previously absent plasmonic functionalities while retaining a compact footprint. Recently for example, Tuniz et al.

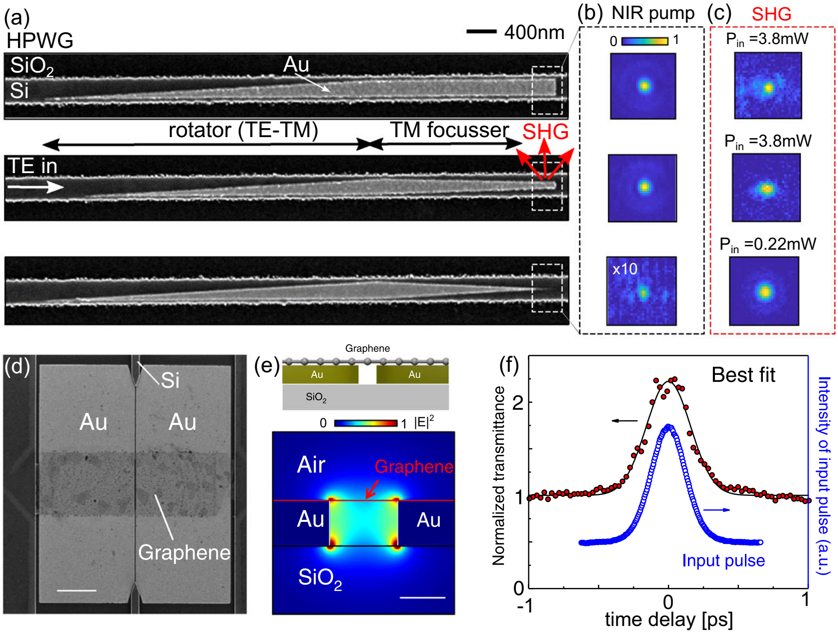

Fig. 21 **a** SEM top view of a post-processed SOI HPWG circuit. It consists of an industry-standard TE ridge waveguide followed by two in-series plasmonic circuit modules: (i) a TE-photonic to TM-plasmonic rotator, and (ii), nano-focusing tips of increasing sharpness. SHG occurs at the tip. **b** Measured scattered light from the tips at **b** at the NIR pump wavelength, and **c** at the SHG wavelength. Images in **b**, **c** are respectively captured under the same conditions, unless otherwise indicated. P_{in}: Incident average power. Note the bright scattered SHG light for the sharpest tip and at low powers, due to nonlinear enhancement. Adapted from Ref. [209] under a Creative Commons license (CC BY 4.0). **d** SEM images of a fabricated photonic-to-plasmonic mode converter and graphene overlayer. Scale bar: 1 μm. **e** Top: schematic of its cross-section side view and associated. Bottom: calculated intensity profile, showing a large overlap between the plasmonic hot-spots and the graphene monolayer. Scale bar: 20 nm. **f** Femtosecond all-optical switching through the waveguide, harnessing graphene saturable absorption (SA), via time-delayed pump-probe experiments. Adapted with permission from Ref. [146], Copyright (2020) Springer Nature

developed a HPWG circuit formed by two back-to-back hybrid plasmonic modules (namely, a plasmonic rotator and focuser, shown in Fig. 21a), both of which were integrated on a standard silicon photonic waveguide. Over the length of the 9 μm HPWG device, the authors show modal rotation (from TE to TM) and subsequent nanofocusing (via a tapered plasmonic tip), which leads to an enhancement of second harmonic generation due to the surface $\chi^{(2)}$ effects of gold. The authors harness the enhancement of nonlinear light generation to experimentally demonstrate a field enhancement of more than 100× scattered from increasingly sharp tips, as shown in Fig. 21b, c, down to an estimated mode area of 100 nm^2. Although the SHG conversion efficiency was only $\sim 10^{-11}$, these proof-of-concept experiments exemplify pathways for enhancing existing networks of photonic circuits with multiple sub-wavelength plasmonic nonlinear functions.

A number of dielectric-plasmonic waveguide circuits, designed ab-initio, have unlocked wavelength-scale all-optical switching, electro-optics, and terahertz detection and generation, as we now discuss.

5.1 All-optical switching

Recently, Ono et al. used nonlinear plasmonic slot waveguides to address the well-known tradeoffs between all-optical switching speeds and associated energy requirements [29,146], using graphene as the nonlinear material in the slot. Their structures interface a silicon photonic circuit and a plasmonic slot waveguide with a graphene layer directly on top of the metal, as shown in Fig. 21a. While two-dimensional materials such as graphene [210] have extreme nonlinear optical properties, the optical interactions are still relatively weak due to the short molecule-scale lengths over which nonlinear interactions occur. The authors overcome this limitation by combining the plasmonic hotspots at the edge of the gold metal (shown in the Fig. 21e calculations) and the high photonic-to-plasmonic efficiency of the plasmonic taper section [211], over micron-scale interaction lengths. Graphene's ultrafast saturable absorption (SA) thereby leads to the transmission of a signal pulse when a control pulse overlapped with it. Figure 21f shows the associated experimental transmission through the entire device as a function of pulse delay, highlighting the ultrafast response time of 260 fs.

5.2 Electro-optics

Several chip-compatible hybrid plasmonic devices that harness the $\chi^{(2)}$ linear electro-optic effect have also been reported, enabling compact, low-power, and high-speed data modulation [151], terahertz detection [150] and generation [212]. Pockels-effect nonlinear modulators compete with those harnessing free-carrier [213], thermo-optic [214], or mechanical effects [215], due to the wide bandwidth and reduced power consumption in a micro-scale physical footprint. The driving physical principles are analogous to those described so far: a dielectric photonic waveguide funnels light to one- or multiple-plasmonic element—most commonly, a nanometre-scale plasmonic slot waveguide—containing a large $\chi^{(2)}$ material [19]. Besides providing a large mode overlap between optical fields and a low-frequency (typically, GHz or THz) fields, the plasmonic slot waveguide is also a capacitor, providing a natural bridge between nano-optics and micro-electronics. Whether it be induced by external electrical signals [194], or external THz radiation [150], electric fields inside the slot can modulate the index change inside the slots, encoded as phase changes of an incoming constant-wave (CW) laser. The outgoing optical signals can then be detected with conventional spectrum analyzers or coherent receivers. The bandwidth of such devices is more than 1 THz, with the dielectric material itself having a response time of a few femtoseconds [194].

In this context, Melyikan et al. [194] reported the first experimental demonstration of a high-speed plasmonics phase modulator (40 Gbit/s) over a 29 μm-length MDM slot waveguide containing an electro-optic polymer. The concept was then extended to a two-arm configuration forming a Mach–Zehnder modulator (MZM), shown in the

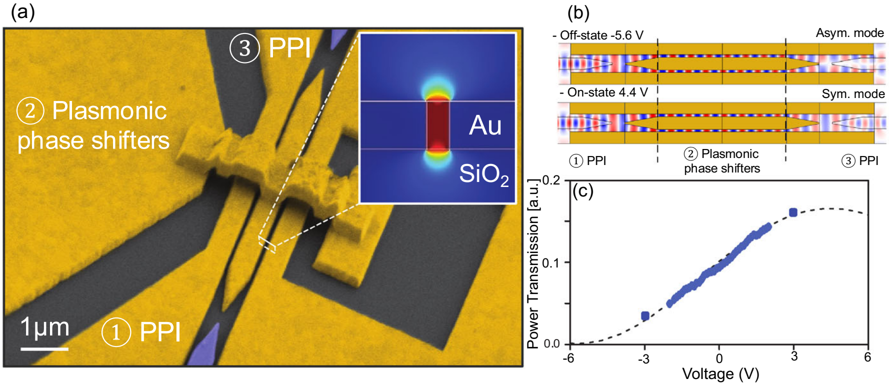

Fig. 22 **a** False-colour SEM micrograph showing a photonic–plasmonic circuit Mach–Zehnder modulator. A suspended bridge connects the gold plasmonic slots to electrical controls, forming a plasmonic phase shifter. Inset: calculated MDM mode of one arm. The photonic-plasmonic-interference (PPI) at output and input converts light from the photonic waveguide into two plasmonic slot waveguide modes, as shown in **b**. Depending on the applied voltage, transmission into the photonic mode can be off (if SPPs in the arms of the MZM are out of phase) or on (so that they are in phase and couple to the photonic guided mode.) **c** Measured (symbols) and modelled (dashed line) optical power transfer function versus applied voltage. Adapted with permission from Ref. [151], Copyright (2015) Springer Nature

SEM micrograph of Fig. 22a, and whose performance is exemplified by the simulations in Fig. 22b. Here, two out-of-phase plasmonic waveguides (“off” states) are brought in phase (“on” states) via external electrical signals, directly encoding the external electrical signals on the incoming laser intensity via the power transfer function shown in Fig. 22c and with 70 GHz bandwidth. In these experiments, the plasmonic slot interfaced with a dielectric waveguide via an adiabatic taper, with the whole process being compatible with CMOS fabrication. In the spirit of relaxing fabrication requirements while maintaining high performance, this concept was used in an all-metallic device surrounded by the same nonlinear polymer [216]. In this case, the polarization of the electric field of the grating-coupled surface plasmon rotates—from the upper surface gold layer into the lateral plasmonic slots—and an external 116 GB/s electrical data stream was encoded into the optical signal. In a more recent resonant-switch design [217], the overall losses of the dielectric-plasmonic modulator were reduced by ensuring that the “on” state remains in the dielectric, while the “off” state couples to the lossy plasmonic mode, thereby harnessing the advantages of both dielectrics and plasmonics. Related designs are increasingly being included on monolithic chips of increasing sophistication [154]. The field of plasmonic-organic hybrid integration is rapidly developing; we point the reader to Refs. [19,152,153] for recent related reviews.

5.3 Terahertz detection and generation

The THz bandwidth associated with the nonlinear electro-optic devices presented above can also be harnessed for all-optical detection of electromagnetic fields at terahertz frequencies. Terahertz radiation is an enabling and rapidly developing multidisciplinary technology serving many diverse areas including security, telecommunications, and sensing [218]. However, as a relatively new technology, THz sources and detectors are less developed, typically bulky due to the relative large millimetre scale wavelengths involved, and are not particularly efficient in interfacing with conventional optical elements and photonic circuitry. Plasmonic nonlinear devices are increasingly bridging these technological gaps using $\chi^{(2)}$ effects. Salamin et al. [150] experimentally demonstrated wirelessly driven plasmonic phase modulator that can directly encode a data from an external millimetre wave (0.06 THz) incident electric field on an optical carrier within an optical waveguide circuit, enhancing the low modal overlap between the incoming field and the optical wave via an appropriately designed resonance. This technology was recently adapted to even higher THz frequencies [219], and formed the basis for a low-footprint monolithic terahertz field detector [220]. This technology is rapidly moving out of the laboratory and into practical settings [221]—for example, Mach–Zehnder plasmonic configurations have been used as wireless THz-to-optical wireless receivers with 0.36 THz 3 dB bandwidth for 50 Gbit/s data streams [222]. Such architectures make terahertz technology more accessible, since it can be interfaced with conventional photonic structures (including optical fibers), and will likely be key in next-generation THz communications and portable low-cost THz detectors and terahertz imaging systems.

The generation of broadband terahertz radiation, on the other hand, most commonly relies on transient currents in a biased photoconductor micro-antenna illuminated by femtosecond pulses [218]. As an alternative, all-optical terahertz sources can use difference frequency generation, a $\chi^{(2)}$ process wherein two intense electric fields at THz-spaced frequencies generate a nonlinear polarization in the medium at the difference frequency. These schemes typically require phase-matching between the terahertz envelope and the beating optical waves, e.g., in mm-thickness crystals [223]. Yao et al. presented a microscale, chip-based structures using two-layer gated graphene heterostructure (each graphene layer separated by AlO_3), placed on top of a SiN_3 waveguide; conceptually, graphene forms an atom-thick plasmonic waveguide with a gate-tuneable permittivity, and large $\chi^{(2)}$. Counter propagating pump and signal photons phase match with the supported graphene plasmons, which can be appropriately externally tuned. Note the extreme properties of the plasmons involved: the generated terahertz plasmons have frequencies of 4–9 THz, and effective wavelength of 460–770 nm, corresponding to $n_{\mathrm{eff}} = 50-120$. Here the conversion efficiency is $\sim 10^{-4}$, limited by the propagation length of the graphene plasmons.

An alternative approach for generating THz radiation is optical rectification (OR), whereby ultrashort optical pulses generate terahertz pulses in a $\chi^{(2)}$ media as a result of the nonlinear interactions between the pulse's constituent THz-bandwidth frequencies [224]. OR has been harnessed to generate terahertz radiation on planar metal nanofilms [225] plasmonic nanoparticle arrays [226], and metamaterial arrays [227] but the best of our knowledge has yet to be reported in photonic-plasmonic waveguides.

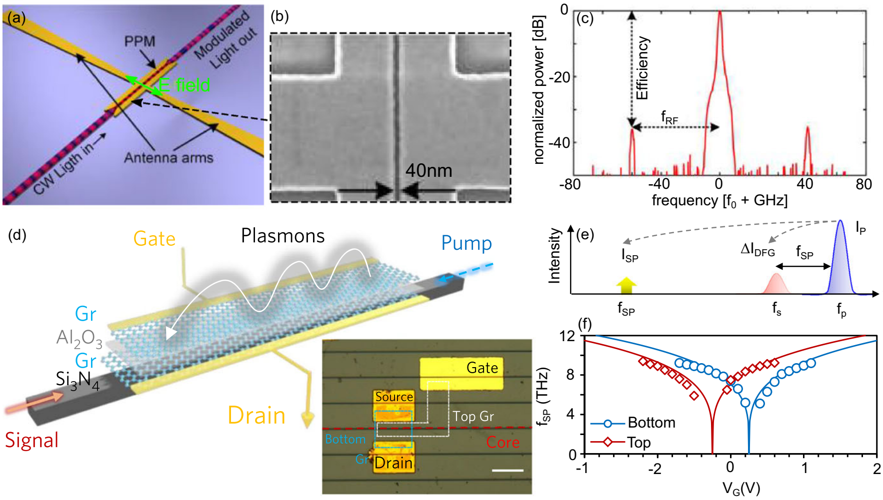

Fig. 23 Example nonlinear plasmonic-photonic circuits for THz detection and generation. **a** Concept schematic of a photonic-plasmonic THz detector. The external THz radiation (green) is collected by the antenna and confined to the plasmonic slot, so that CW light from the silicon WG is converted to SPPs, whose phase is modulated by the plasmonic phase modulator (PM) via the THz field. **b** SEM image of the 40 nm wide plasmonic slot used in the experiment. **c** Measured optical response of the device, showing the sidebands at the modulating 0.06 THz frequency. Adapted with permission from Ref. [150]. Copyright (2015) American Chemical Society. **d** Schematic of a two-layer graphene hybrid plasmonic circuit (GHPC) for THz generation via SPPs, using counter-pumped $\chi^{(2)}$ difference frequency generation (DFG). Inset: Top-view microscope image of the GHPC. Scale bar: 50 μm. **e** Schematic of DFG process. A phase-matched (counter-propagating) pump and signal at respective frequency f_P and f_S produce a graphene plasmon with frequency f_{SP}. Phase matching can be tuned via an external voltage V_G, which modifies the graphene dispersion. **f** Observed frequency f_{SP} as a function of the voltage on the top- (red) and bottom- (blue) graphene layer. Adapted with permission from Ref. [212], Copyright (2018) Springer Nature

5.4 Surface-enhanced Raman scattering

Finally, we mention one of the most widely-used nonlinear effects in plasmonics: Surface-Enhanced Raman Scattering (SERS) [228], wherein the large field enhancements enabled by plasmonics boosts the spectral fingerprints emerging from inelastic scattering processes between light and a molecule's vibrational modes. For many decades, SERS used localized, non-guided surface plasmon polaritons, e.g., via rough surfaces [229] and nanoparticles [230]. More recently, "remote" SERS has been developed [231–233], combining propagating SPPs (e.g., on a nanowire) with neighbouring localized SPPs, e.g., at its extremity. In such nonlinear plasmonic structures, the objective is to locally generate extreme fields in the smallest possible volume, and detect the Raman-shifted fingerprint at longer wavelengths; conventional guided guided surface plasmons generally do not provide sufficient enhancement, and plasmonic tips (i.e., tapered and terminated plasmonic waveguides) are used [234]. These provide the important advantage of a background-free nonlinear Raman signal originating from a nanoscale volume of interest. More recently, chip-compatible SERS devices that integrate plasmonic antennas [59,235] and plasmonic slot waveguides [236,237] have

Table 2 Summary of selected on-chip nonlinear plasmonic experiments discussed, including the structure considered, the nonlinear effect observed, the estimated/reported conversion efficiency η (italic) or phase shift $\boldsymbol{\Delta\phi}$ (bold), the nominal physical device area A_d and device length L_d, and the dominant nonlinear material involved in the nonlinear process

Structure	Effect	η or $\Delta\phi(rad)$	A_d (μm^2)	L_d (μm)	N.L. material
SR-SPP [176]	SHG	$\sim 10^{-14}$	0.0075	20	Gold
SR-SPP [176]	THG	$\sim 10^{-13}$	0.0075	20	Gold
SR-SPP [180]	FWM	1×10^{-5}	0.008	20	Gold
SPP [185]	THG	2.3×10^{-5}	0.4	<10	Silicon
HPWG [158]	SPM	10^{-8}	0.12	10	Silicon
MDM [127]	FWM	4.7×10^{-2}	0.0005	2	MEH-PPV
HPWG [209]	SHG	10^{-11}	0.1–0.0005	9	Gold
HPWG [188]	SHG	4×10^{-5}	0.1	5	CdSe
HPWG [189]	SHG/SFG	$10^{-6}/10^{-5}$	0.03	1–15	AlGaInP
MDM [146]	SA	–	0.0006	10	Graphene
MDM [151]	EO mod.	$\boldsymbol{\pi/2}$	0.04	10	DLD-164
MDM [150]	THz det.	**0.0323**	0.01	50	DLD-164
SPP [212]	THz gen.	10^{-4}	0.7250	60	Graphene

All pumps are in the NIR

also emerged, whose modes are optimized to ensure the dominant Raman contribution comes from the slot by limiting the modal overlap with the dielectric waveguide [237]. Such sensors will also benefit from more efficient plasmonic coupling designs concentrating light to ever decreasing nanoscale volumes. We refer the reader to Ref. [228] for a recent review on SERS, which includes a comprehensive section on waveguide-based approaches.

6 Nonlinear quantum plasmonics

Photonics is one of the more promising platforms underpinning next-generation quantum-based technologies, e.g., quantum computing [130,238], secure communications [239], and quantum-enhanced metrology [240]. Light has been a workhorse for investigating quantum mechanics since the early days [241,242]; most recently, integrated optical platforms are playing an increasingly important role, promising to provide a noise-free monolithic means of conveniently and reliably generating, manipulating, and detecting single- and entangled-photons [243–245]. In keeping with the theme of this review, we now briefly discuss nonlinear plasmonics for quantum applications in the specific context of integrated waveguides.

The nonlinear effects considered thus far operate at high (pump) photon numbers and weak nonlinearities (grey box of Fig. 24 [246]). A material's $\chi^{(2)}$ or $\chi^{(3)}$ nonlinearity can also produce entangled photon states at frequencies far from the pump, via spontaneous parametric downconversion (SPDC) and spontaneous four-

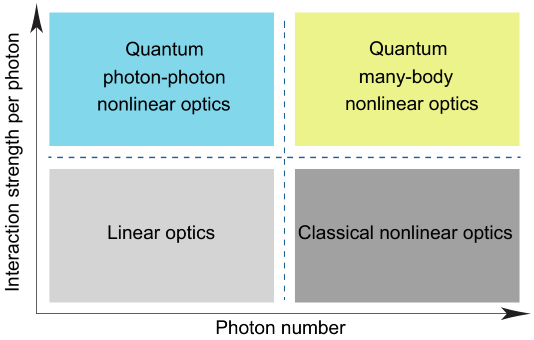

Fig. 24 Summary schematic of classical- and quantum-light regimes on the basis of photon number and interaction strength per photon. Linear optics (light grey): weak interaction strength per photon and low photon numbers. Classical nonlinear optics (dark grey) relies on higher photon numbers, but materials' intrinsic interaction strength per photon is low. Quantum nonlinear enters the picture at larger interaction strengths per photons becomes large: if the photon number is small, photon–photon nonlinear optics takes place at the quantum emitter level (blue); if the photon number is large, and the interaction strength per photon is large, many photons interact simultaneously to produce strongly correlated many-body states. Adapted with permission from Ref. [246], Copyright (2018) Springer Nature

wave mixing (SFWM) respectively [244]. On the other hand, nonlinear effects at the single-photon level provide a means of generating quantum states and rely on strong interaction strengths with matter *per photon*, as shown in the blue box of Fig. 24. At low photon numbers, the nonlinear interaction between two photons can be mediated by each photon strongly interacting with a quantum emitter (blue box). Here, typical schemes require photons to interact sequentially with a quantum emitter [247–249]—the presence of the first photon is imprinted on the quantum emitter by changing its internal state, which influences the second photon, so that the quantum emitter induces a photon-photon interaction. Reaching the realm of quantum many-body nonlinear optics (yellow box) can open the door for creating entangled many-body states of photons. This requires both a large number of photons and a large nonlinearity per photon. One proposal has shown that many-body states of light can be generated by unidirectionally coupling many quantum emitters to a waveguide [250]. This can in principle also be achieved in plasmonic waveguides [251], although practical implementations may be limited by loss. Another possible route to reach this limit can potentially be achieved by using the material response of a given waveguide configuration, analogously to the requirement of a large nonlinear phase shift (Eq. (11)).

What role, if any, can nonlinear plasmonics play in all this? One advantage is that that quantum nonlinear effects are more likely when the effective volume occupied by photons approaches the deep sub-wavelength scale, provided by nano-focused plasmonic modes. Complementarily, plasmonic nanostructures increase the density of available optical states [252], increasing the probability of photon emission, so that photons emitted by a quantum emitter can couple to surface plasmon modes near-deterministically [253]. This requirement is key both for efficient on-chip photon sources and for strong photon–photon nonlinearities [254]. However, care should be taken in ensuring that the associated enhancement in emission does not couple to a non-radiating channel (e.g., loss due to damping): proper emitter placement near the metal is extremely important to avoid detrimental quenching effects [252]. At a fundamental level, any useful single photon state is immediately destroyed by the loss of any photon, which often raises eyebrows when suggesting lossy plasmonic systems as viable quantum platforms.

However, a number of recent experiments of on-chip quantum emitters [255], complemented by analytical theories [256] indicate that quantum plasmonics [257,258] can enhance the capabilities of all-dielectric architectures [252,259,260]. With ever improving circuit designs for coupling dielectric waveguide modes to single quantum emitters [261], one advantage of plasmonically coupled emitters over their all-dielectric counterparts is their broadband, non-resonant, enhanced emission rate [256] and thus shorter emitter lifetime, which could facilitate the generation of a coherent source of single photons that is required for most quantum protocols. One perspective [262] is that plasmonic devices reduce the spontaneous emission time t_{sp} times below the characteristic dephasing times t_{deph} at room temperature; dielectric-based approaches instead increase t_{deph} by reducing the temperature as illustrated in Fig. 25a. An example feasibility study of efficient room-temperature sources of indistinguishable single photons using plasmonic cavities was reported in Ref. [263].

Several recent experiments have shown the promise of photonic-plasmonic quantum architectures. For example, Gong et al. used three-dimensional guided plasmonic nanofocusing on a deterministally positioned quantum emitter to enhance its spontaneous emission by a factor of ~ 22. Most recently, a single-molecule nonlinearity was experimentally shown via a dye molecule inside a plasmonic waveguide [264], and the resulting single-photon fluoresence showed a one-order of magnitude reduction in emission lifetime compared to the non-plasmonic case. Grandi et al. [265] included a single molecule into a hybrid gap plasmon waveguide akin to that shown in Fig. 19a, showing single molecule emission from the output of the entire device, which originated from the plasmonic nano-gap, although the plasmonic gap of 200 nm was too wide to reduce the decay rate. With ever-improving techniques for deterministic placements of quantum emitters [266], and the ability to controllably pattern nanometre-scale metallic channels [267], similar geometries might provide the building block for fast room-temperature single-photon emitters that coupled to low-loss dielectric guides assited by plasmonics, as per the schematic of Fig. 10b.

Guided-wave multiphoton nonlinearities have been recently theoretically and experimentally revisited for guided lossy media in the context of quantum applications. In 2016, Poddubny et al. [269] developed general theoretical framework of integrated nonlinear parametric photon-plasmons guided waves, accounting for material dispersion and losses. Such realistic studies suggested relatively high efficiency of 70%, and even presented novel enhancement mechanisms due to the anisotropic eigenmode topology of metal/dielectric multilayers. New toolkits for dealing with nonlinear quantum processes in lossy media are continuously being developed [270,271]. Experiments that rely on nonlinear plasmonics processes to generate quantum states are rare: guiding entangeld multi-photon states through the lossy media too easily destroys them. Recent efforts have attempted to use guided surface plasmon polaritons to enhance spontaneous parametric downconversion [272], and some initial steps have

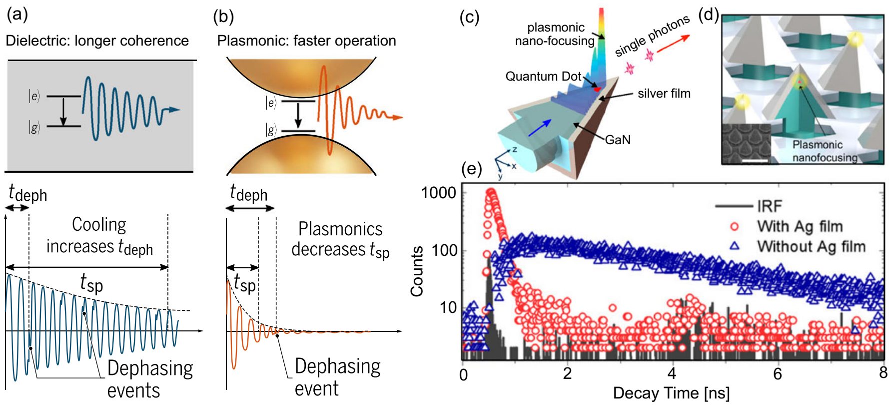

Fig. 25 **a** Schematic illustrating plasmonic speedup of single-photon emitters. “Coherent” photons from quantum emitters occur from spontaneous transitions from an excited state $|e>$ to a ground state $|g>$. Coherence requires that the spontaneous emission time t_{sp} be shorter than dephasing events with characteristic time scale t_{deph}. Dielectrics optain long t_{deph} by cooling; plasmonics achieve short t_{sp} via a fast spontaneous emission rate (i.e., large Purcell factor). Adapted from Ref. [262]. Reprinted with permission from AAAS. **b** Schematic of a quantum dot array deterministically placed near a plasmonic nanofocus. Inset: SEM image of the fabricated device (Scale bar: 500 nm). **d** Concept schematic of device principle: a three-dimensional nanofocused plasmonic mode is aligned with a single emitter at the nanofocus. **e** Example decay dynamics of the emitter: the decay time is 4 ns for the single QD without a silver film (blue), and 0.14 ns for the QD with a silver film (red). (Black line: instrument response function.) Adapted from Ref. [268]. Copyright (2015) National Academy of Sciences

been made [273]; stronger nonlinearities, lower losses, and hybrid waveguide designs [271], could potentially overcome current limitations.

Although light-matter interactions are weaker in all-dielectric structures, the library of photonic elements (e.g., couplers, splitters, etc.) is better established, more flexible, and thus provides a more convenient platform for more advanced early experiments. Integrated plasmonics could potentially miniaturize these systems to the nanoscale, lower the energy requirements, and provide faster room temperature operation; currently however, the majority of quantum photonic experiments are still confined to research laboratories, where the absence of such characteristics do not preclude fundamental studies of chip-scale quantum interactions in these early research stages. Plasmonics-based approaches might however become the go-to later-generation technology for quantum photonic architectures, once they become more widespread.

7 Conclusions and outlook

We have provided an introductory overview of nonlinear plasmonic in guided wave systems, which we believe will play an important role in the next generation of compact, ultrafast, low-power photonic integrated devices. We have mentioned a few notable applications, including all-optical switching, terahertz generation, electro-optics, single-molecule sensing, and quantum optics, but this list is by no means exhaustive [51].

While plasmonics-based guided-wave structures are capable of extreme nonlinear optics inside deep sub-diffraction volumes, they push nanofabrication demands to the limit of current capabilities, and demand a lot from the materials involved—often operating at the edge of their breaking point (albeit at lower powers). However, recent years have been marked by the explosion of a huge family of highly nonlinear two-dimensional (2D) materials, some of which have been mentioned here. The most famous of these, graphene, supports plasmonic modes [274–276] and can also act as a highly nonlinear medium for enhancing dielectric waveguides [277]. 2D materials have large nonlinear susceptibilities, but under standard illumination the interaction length is only a few atoms thick: guided-wave plasmonics [278] can provide a way of concentrating the light to a volume comparable to the thickness of the material itself—not to mention interaction lengths orders of magnitude longer than the width of a few atoms! We have already seen the power of these combined features in the device of Fig. 21d–f, although a complete description at such scales must also account for non-local effects [279]. The role of plasmonics in enhancing the performance of such 2D materials has been the topic of recent reviews [280,281], and it is only a matter of time before guided-wave hybrid nonlinear plasmonic devices, enhanced by 2D materials, integrate with PICs to unlock record-level ultrafast nonlinear effects in an accessible manner. Photonic-plasmonic-2D circuits are now starting to appear [282], albeit in a different context, and current fabrication capabilities enable a scalable approach for including 2D materials on large-area waveguides [283,284].

Complementary to approaching improvements from a material perspective, it may be that other waveguide geometries may provide enhanced nonlinear interactions as a pathway for investigating new physics—for example, non-Hermitian systems [285], accessible via plasmonic waveguides [286], exhibit slow light effects at their exceptional point [287], where they are also extremely sensitive to their environment [288]. Related concepts [289] might prove a worthwhile avenue for chip-based nonlinear sensing of nanoscale events.

In conclusion we hope that, as alternate avenues for nonlinear enhancement emerge, as fabrication techniques develop, and as material science further matures, this tutorial-style review may provide a useful introductory conceptual toolkit for approaching this exciting and powerful field.

Acknowledgements The author sincerely thanks C. Martijn de Sterke, Guangyuan (Clark) Li, Gordon H. Li, Stefano Palomba, Fernando J. Diaz, and Loris Marini for countless stimulating discussions on several topics contained in this review. The author also thanks Sahand Mahmoodian for valuable insights on nonlinear quantum photonics, and Birgit Stiller for providing feedback on a version of this manuscript. This work was in part supported by the University of Sydney Postdoctoral Fellowship scheme at the University of Sydney Nano Institute. The author is the recipient of an Australian Research Council Discovery Early Career Award (project number DE200101041) funded by the Australian Government.

References

1. S.E. Miller, Integrated optics: an introduction. Bell Syst. Tech. J. **48**(7), 2059–2069 (1969)
2. M. Smit, K. Williams, J. Van Der Tol, Past, present, and future of InP-based photonic integration. APL Photonics **4**(5), 050901 (2019)
3. X. Chen, M.M. Milosevic, S. Stanković, S. Reynolds, T.D. Bucio, K. Li, D.J. Thomson, F. Gardes, G.T. Reed, The emergence of silicon photonics as a flexible technology platform. Proc. IEEE **106**(12), 2101–2116 (2018)
4. D. Dai, J. Bauters, J.E. Bowers, Passive technologies for future large-scale photonic integrated circuits on silicon: polarization handling, light non-reciprocity and loss reduction. Light Sci. Appl. **1**(3), e1 (2012)
5. W. Bogaerts, D. Pérez, J. Capmany, D.A. Miller, J. Poon, D. Englund, F. Morichetti, A. Melloni, Programmable photonic circuits. Nature **586**(7828), 207–216 (2020)
6. T.L. Koch, U. Koren, Semiconductor photonic integrated circuits. IEEE J. Quantum Electron. **27**(3), 641–653 (1991)
7. F. Kish, R. Nagarajan, D. Welch, P. Evans, J. Rossi, J. Pleumeekers, A. Dentai, M. Kato, S. Corzine, R. Muthiah et al., From visible light-emitting diodes to large-scale III-V photonic integrated circuits. Proc. IEEE **101**(10), 2255–2270 (2013)
8. A. Boes, B. Corcoran, L. Chang, J. Bowers, A. Mitchell, Status and potential of lithium niobate on insulator (LNOI) for photonic integrated circuits. Laser Photonics Rev. **12**(4), 1700256 (2018)
9. P. Dong, Y.-K. Chen, G.-H. Duan, D.T. Neilson, Silicon photonic devices and integrated circuits. Nanophotonics **3**(4–5), 215–228 (2014)
10. A. Rahim, E. Ryckeboer, A.Z. Subramanian, S. Clemmen, B. Kuyken, A. Dhakal, A. Raza, A. Hermans, M. Muneeb, S. Dhoore et al., Expanding the silicon photonics portfolio with silicon nitride photonic integrated circuits. J. Lightwave Technol. **35**(4), 639–649 (2017)
11. C. Kopp, S. Bernabe, B.B. Bakir, J.-M. Fedeli, R. Orobtchouk, F. Schrank, H. Porte, L. Zimmermann, T. Tekin, Silicon photonic circuits: on-cmos integration, fiber optical coupling, and packaging. IEEE J. Sel. Topics Quantum Electron. **17**(3), 498–509 (2010)
12. D.J. Blumenthal, Photonic integration for UV to IR applications. APL Photonics **5**(2), 020903 (2020)
13. C.R. Doerr, Silicon photonic integration in telecommunications. Front. Phys. **3**, 37 (2015)
14. J.L. O'Brien, Optical quantum computing. Science **318**(5856), 1567–1570 (2007)
15. J.-H. Kim, S. Aghaeimeibodi, J. Carolan, D. Englund, E. Waks, Hybrid integration methods for on-chip quantum photonics. Optica **7**(4), 291–308 (2020)
16. A.Z. Subramanian, E. Ryckeboer, A. Dhakal, F. Peyskens, A. Malik, B. Kuyken, H. Zhao, S. Pathak, A. Ruocco, A. De Groote et al., Silicon and silicon nitride photonic circuits for spectroscopic sensing on-a-chip. Photonics Res. **3**(5), B47–B59 (2015)
17. M Alexander Schmidt, A. Argyros, F. Sorin, Hybrid optical fibers-an innovative platform for in-fiber photonic devices. Adv. Optical Mater. **4**(1), 13–36 (2016)
18. J. Marks, InP multi-project wafer. Creative Commons Attribution-Share Alike 4.0 International (2017). https://creativecommons.org/licenses/by-sa/4.0/
19. W. Heni, C. Haffner, D.L. Elder, A.F. Tillack, Y. Fedoryshyn, R. Cottier, Y. Salamin, C. Hoessbacher, U. Koch, B. Cheng et al., Nonlinearities of organic electro-optic materials in nanoscale slots and implications for the optimum modulator design. Optics Express **25**(3), 2627–2653 (2017)
20. P. Ma, Y. Salamin, B. Baeuerle, A. Josten, W. Heni, A. Emboras, J. Leuthold, Plasmonically enhanced graphene photodetector featuring 100 Gbit/s data reception, high responsivity, and compact size. ACS Photonics **6**(1), 154–161 (2018)
21. Y. Salamin, P. Ma, B. Baeuerle, A. Emboras, Y. Fedoryshyn, W. Heni, B. Cheng, A. Josten, J. Leuthold, 100 GHz plasmonic photodetector. ACS Photonics **5**(8), 3291–3297 (2018)
22. S. Chung, H. Abediasl, H. Hashemi, 15.4 a 1024-element scalable optical phased array in 0.18 μm SOI CMOS. in *2017 IEEE International Solid-State Circuits Conference (ISSCC)*, pp. 262–263. IEEE (2017)
23. C. Sun, M.T. Wade, Y. Lee, J.S. Orcutt, L. Alloatti, M.S. Georgas, A.S. Waterman, J.M. Shainline, R.R. Avizienis, S. Lin et al., Single-chip microprocessor that communicates directly using light. Nature **528**(7583), 534–538 (2015)
24. D.W. Kim, M.H. Lee, Y. Kim, K.H. Kim, Planar-type polarization beam splitter based on a bridged silicon waveguide coupler. Optics Express **23**(2), 998–1004 (2015)

25. R. Marchetti, C. Lacava, L. Carroll, K. Gradkowski, P. Minzioni, Coupling strategies for silicon photonics integrated chips. Photonics Res. **7**(2), 201–239 (2019)
26. W.D. Sacher, T. Barwicz, B.J. Taylor, J.K. Poon, Polarization rotator-splitters in standard active silicon photonics platforms. Optics Express **22**(4), 3777–3786 (2014)
27. M. Piekarek, D. Bonneau, S. Miki, T. Yamashita, M. Fujiwara, M. Sasaki, H. Terai, M.G. Tanner, C.M. Natarajan, R.H. Hadfield et al., High-extinction ratio integrated photonic filters for silicon quantum photonics. Optics Lett. **42**(4), 815–818 (2017)
28. L. Liao, A. Liu, R. Jones, D. Rubin, D. Samara-Rubio, O. Cohen, M. Salib, M. Paniccia, Phase modulation efficiency and transmission loss of silicon optical phase shifters. IEEE J. Quantum Electron. **41**(2), 250–257 (2005)
29. S.M. Hendrickson, A.C. Foster, R.M. Camacho, B.D. Clader, Integrated nonlinear photonics: emerging applications and ongoing challenges. J. Optical Soc. Am. B **31**(12), 3193–3203 (2014)
30. N. Singh, D.D. Hudson, Y. Yu, C. Grillet, S.D. Jackson, A. Casas-Bedoya, A. Read, P. Atanackovic, S.G. Duvall, S. Palomba et al., Midinfrared supercontinuum generation from 2 to 6 μm in a silicon nanowire. Optica **2**(9), 797–802 (2015)
31. R.W. Boyd, *Nonlinear Optics* (Academic press, New York, 2019)
32. B.J. Eggleton, B. Luther-Davies, K. Richardson, Chalcogenide photonics. Nat. Photonics **5**(3), 141–148 (2011)
33. M.A. Foster, K.D. Moll, A.L. Gaeta, Optimal waveguide dimensions for nonlinear interactions. Optics Express **12**(13), 2880–2887 (2004)
34. G.P. Agrawal, Nonlinear fiber optics: its history and recent progress. J. Optical Soc. Am. B **28**(12), A1–A10 (2011)
35. L.F. Mollenauer, R.H. Stolen, J.P. Gordon, Experimental observation of picosecond pulse narrowing and solitons in optical fibers. Phys. Rev. Lett. **45**(13), 1095–1098 (1980)
36. J.M. Dudley, G. Genty, S. Coen, Supercontinuum generation in photonic crystal fiber. Rev. Mod. Phys. **78**(4), 1135 (2006)
37. B. Kuyken, F. Leo, S. Clemmen, U. Dave, R. Van Laer, T. Ideguchi, H. Zhao, X. Liu, J. Safioui, S. Coen et al., Nonlinear optical interactions in silicon waveguides. Nanophotonics **6**(2), 377–392 (2017)
38. A. Rahim, T. Spuesens, R. Baets, W. Bogaerts, Open-access silicon photonics: Current status and emerging initiatives. Proc. IEEE **106**(12), 2313–2330 (2018)
39. Y. Shani, C. Henry, R. Kistler, K. Orlowsky, D. Ackerman, Efficient coupling of a semiconductor laser to an optical fiber by means of a tapered waveguide on silicon. Appl. Phys. Lett. **55**(23), 2389–2391 (1989)
40. P. Cheben, R. Halir, J.H. Schmid, H.A. Atwater, D.R. Smith, Subwavelength integrated photonics. Nature **560**(7720), 565–572 (2018)
41. S.A. Maier, *Plasmonics: Fundamentals and Applications* (Springer, New York, 2007)
42. S.A. Maier, M.L. Brongersma, P.G. Kik, S. Meltzer, A.A. Requicha, H.A. Atwater, Plasmonics-a route to nanoscale optical devices. Adv. Mater. **13**(19), 1501–1505 (2001)
43. V.J. Sorger, R.F. Oulton, R.-M. Ma, X. Zhang, Toward integrated plasmonic circuits. MRS Bull. **37**(8), 728–738 (2012)
44. P.R. West, S. Ishii, G.V. Naik, N.K. Emani, V.M. Shalaev, A. Boltasseva, Searching for better plasmonic materials. Laser Photonics Rev. **4**(6), 795–808 (2010)
45. N. Maccaferri, S. Meuret, N. Kornienko, D. Jariwala, Speeding up nanoscience and nanotechnology with ultrafast plasmonics. Nano Lett. **20**(8), 5593–5596 (2020). PMID: 32787183
46. D.A. Miller, Are optical transistors the logical next step? Nat. Photonics **4**(1), 3–5 (2010)
47. E. Hutter, J.H. Fendler, Exploitation of localized surface plasmon resonance. Adv. Mater. **16**(19), 1685–1706 (2004)
48. S. Palomba, M. Danckwerts, L. Novotny, Nonlinear plasmonics with gold nanoparticle antennas. J. Optics A Pure Appl. Optics **11**(11), 114030 (2009)
49. E. Rahimi, R. Gordon, Nonlinear plasmonic metasurfaces. Adv. Optical Mater. **6**(18), 1800274 (2018)
50. M. Lapine, I.V. Shadrivov, Y.S. Kivshar, Colloquium: nonlinear metamaterials. Rev. Mod. Phys. **86**(3), 1093 (2014)
51. M. Kauranen, A.V. Zayats, Nonlinear plasmonics. Nat. Photonics **6**(11), 737–748 (2012)
52. P.-Y. Chen, C. Argyropoulos, A. Alù, Enhanced nonlinearities using plasmonic nanoantennas. Nanophotonics **1**(3–4), 221–233 (2012)

53. J. Butet, P.-F. Brevet, O.J. Martin, Optical second harmonic generation in plasmonic nanostructures: from fundamental principles to advanced applications. ACS Nano **9**(11), 10545–10562 (2015)
54. N. Panoiu, W. Sha, D. Lei, G. Li, Nonlinear optics in plasmonic nanostructures. J. Optics **20**(8), 083001 (2018)
55. Y. Fang, M. Sun, Nanoplasmonic waveguides: towards applications in integrated nanophotonic circuits. Light Sci. Appl. **4**(6), e294 (2015)
56. Z. Han, S.I. Bozhevolnyi, Radiation guiding with surface plasmon polaritons. Reports on Progress in Physics **76**(1), 016402 (2012)
57. N. Kinsey, M. Ferrera, V. Shalaev, A. Boltasseva, Examining nanophotonics for integrated hybrid systems: a review of plasmonic interconnects and modulators using traditional and alternative materials. J. Optical Soc. Am. B **32**(1), 121–142 (2015)
58. M.Z. Alam, J.S. Aitchison, M. Mojahedi, A marriage of convenience: Hybridization of surface plasmon and dielectric waveguide modes. Laser Photonics Rev. **8**(3), 394–408 (2014)
59. F. Peyskens, A. Dhakal, P. Van Dorpe, N. Le Thomas, R. Baets, Surface enhanced raman spectroscopy using a single mode nanophotonic-plasmonic platform. ACS Photonics **3**(1), 102–108 (2016)
60. C. Delacour, S. Blaize, P. Grosse, J.M. Fedeli, A. Bruyant, R. Salas-Montiel, G. Lerondel, A. Chelnokov, Efficient directional coupling between silicon and copper plasmonic nanoslot waveguides: toward metal-oxide-silicon nanophotonics. Nano Lett. **10**(8), 2922–2926 (2010)
61. A. Tuniz, M.A. Schmidt, Broadband efficient directional coupling to short-range plasmons: towards hybrid fiber nanotips. Optics Express **24**(7), 7507–7524 (2016)
62. D. Pile, D.K. Gramotnev, Adiabatic and nonadiabatic nanofocusing of plasmons by tapered gap plasmon waveguides. Appl. Phys. Lett. **89**(4), 041111 (2006)
63. M.P. Nielsen, L. Lafone, A. Rakovich, T.P. Sidiropoulos, M. Rahmani, S.A. Maier, R.F. Oulton, Adiabatic nanofocusing in hybrid gap plasmon waveguides on the silicon-on-insulator platform. Nano Lett. **16**(2), 1410–1414 (2016)
64. G. Veronis, S. Fan, Theoretical investigation of compact couplers between dielectric slab waveguides and two-dimensional metal-dielectric-metal plasmonic waveguides. Optics Express **15**(3), 1211–1221 (2007)
65. X.-W. Chen, V. Sandoghdar, M. Agio, Highly efficient interfacing of guided plasmons and photons in nanowires. Nano Lett. **9**(11), 3756–3761 (2009)
66. S. Paul, M. Ray, Plasmonic switching and bistability at telecom wavelength using the subwavelength nonlinear cavity coupled to a dielectric waveguide: A theoretical approach. J. Appl. Phys. **120**(20), 203102 (2016)
67. Z. Chai, Y. Zhu, X. Hu, X. Yang, Z. Gong, F. Wang, H. Yang, Q. Gong, On-chip optical switch based on plasmon-photon hybrid nanostructure-coated multicomponent nanocomposite. Adv. Optical Mater. **4**(8), 1159–1166 (2016)
68. C. Huang, C.M. de Sterke, A. Tuniz, Simple model for orthogonal and angled coupling in dielectric-plasmonic waveguides. Optics Express **27**(15), 20444–20455 (2019)
69. A. Andryieuski, A.V. Lavrinenko, Nanocouplers for infrared and visible light. Adv. OptoElectron. **2012**, 839747 (2012)
70. A. Tuniz, M.A. Schmidt, Interfacing optical fibers with plasmonic nanoconcentrators. Nanophotonics **7**(7), 1279–1298 (2018)
71. A. Krasnok, M. Tymchenko, A. Alù, Nonlinear metasurfaces: a paradigm shift in nonlinear optics. Mater. Today **21**(1), 8–21 (2018)
72. B. Esembeson, M.L. Scimeca, T. Michinobu, F. Diederich, I. Biaggio, A high-optical quality supramolecular assembly for third-order integrated nonlinear optics. Adv. Mater. **20**(23), 4584–4587 (2008)
73. S. Martin, D. Bradley, P. Lane, H. Mellor, P. Burn, Linear and nonlinear optical properties of the conjugated polymers PPV and MEH-PPV. Phys. Rev. B **59**(23), 15133 (1999)
74. J. Burke, G. Stegeman, T. Tamir, Surface-polariton-like waves guided by thin, lossy metal films. Phys. Rev. B **33**(8), 5186 (1986)
75. R. Zia, M.D. Selker, P.B. Catrysse, M.L. Brongersma, Geometries and materials for subwavelength surface plasmon modes. J. Optical Soc. Am. A **21**(12), 2442–2446 (2004)
76. A.D. Rakić, A.B. Djurišić, J.M. Elazar, M.L. Majewski, Optical properties of metallic films for vertical-cavity optoelectronic devices. Appl. Optics **37**(22), 5271–5283 (1998)
77. G.H.Y. Li, C.M. de Sterke, A. Tuniz, Omnidirectional field enhancements drive giant nonlinearities in epsilon-near-zero waveguides. Optics Lett. **45**(23), 6514–6517 (2020)

78. C. Monat, C.M. de Sterke, B.J. Eggleton, Slow light enhanced nonlinear optics in periodic structures. J. Optics **12**(10), 104003 (2010)
79. V.S. Afshar, T. Monro, C.M. de Sterke, Understanding the contribution of mode area and slow light to the effective Kerr nonlinearity of waveguides. Optics Express **21**(15), 18558–18571 (2013)
80. G. Agrawal, *Nonlinear Fiber Optics* (Academic Press, New York, 2012)
81. P. Berini, Long-range surface plasmon polaritons. Adv. Optics Photonics **1**(3), 484–588 (2009)
82. G. Li, C.M. de Sterke, S. Palomba, Figure of merit for Kerr nonlinear plasmonic waveguides. Laser Photonics Rev. **10**(4), 639–646 (2016)
83. G. Veronis, S. Fan, Modes of subwavelength plasmonic slot waveguides. J. Lightw. Technol. **25**(9), 2511–2521 (2007)
84. A.R. Davoyan, I.V. Shadrivov, A.A. Zharov, D.K. Gramotnev, Y.S. Kivshar, Nonlinear nanofocusing in tapered plasmonic waveguides. Phys. Rev. Lett. **105**(11), 116804 (2010)
85. E. Feigenbaum, M. Orenstein, Plasmon-soliton. Optics Lett. **32**(6), 674–676 (2007)
86. L. Chen, J. Shakya, M. Lipson, Subwavelength confinement in an integrated metal slot waveguide on silicon. Optics Lett. **31**(14), 2133–2135 (2006)
87. C. Koos, P. Vorreau, T. Vallaitis, P. Dumon, W. Bogaerts, R. Baets, B. Esembeson, I. Biaggio, T. Michinobu, F. Diederich et al., All-optical high-speed signal processing with silicon-organic hybrid slot waveguides. Nat. Photonics **3**(4), 216–219 (2009)
88. M. Z. Alam, J. Meier, J. S. Aitchison, M. Mojahedi, Super mode propagation in low index medium. in *Quantum Electronics and Laser Science Conference* (Optical Society of America, 2007)
89. R.F. Oulton, V.J. Sorger, D. Genov, D. Pile, X. Zhang, A hybrid plasmonic waveguide for subwavelength confinement and long-range propagation. Nat. Photonics **2**(8), 496–500 (2008)
90. M.Z. Alam, J. Meier, J.S. Aitchison, M. Mojahedi, Propagation characteristics of hybrid modes supported by metal-low-high index waveguides and bends. Optics Express **18**(12), 12971–12979 (2010)
91. F. Diaz, G. Li, C.M. de Sterke, B. Kuhlmey, S. Palomba, Kerr effect in hybrid plasmonic waveguides. J. Optical Soc. Am. B **33**(5), 957–962 (2016)
92. L. Novotny, C. Hafner, Light propagation in a cylindrical waveguide with a complex, metallic, dielectric function. Phys. Rev. E **50**(5), 4094 (1994)
93. E. Moreno, S.G. Rodrigo, S.I. Bozhevolnyi, L. Martín-Moreno, F. García-Vidal, Guiding and focusing of electromagnetic fields with wedge plasmon polaritons. Phys. Rev. Lett. **100**(2), 023901 (2008)
94. S.I. Bozhevolnyi, V.S. Volkov, E. Devaux, T.W. Ebbesen, Channel plasmon-polariton guiding by subwavelength metal grooves. Phys. Rev. Lett. **95**(4), 046802 (2005)
95. B. Steinberger, A. Hohenau, H. Ditlbacher, A. Stepanov, A. Drezet, F. Aussenegg, A. Leitner, J. Krenn, Dielectric stripes on gold as surface plasmon waveguides. Appl. Phys. Lett. **88**(9), 094104 (2006)
96. T. Holmgaard, J. Gosciniak, S.I. Bozhevolnyi, Long-range dielectric-loaded surface plasmon-polariton waveguides. Optics Express **18**(22), 23009–23015 (2010)
97. V.S. Volkov, Z. Han, M.G. Nielsen, K. Leosson, H. Keshmiri, J. Gosciniak, O. Albrektsen, S.I. Bozhevolnyi, Long-range dielectric-loaded surface plasmon polariton waveguides operating at telecommunication wavelengths. Optics Lett. **36**(21), 4278–4280 (2011)
98. G.I. Stegeman, J.D. Valera, C.T. Seaton, J. Sipe, A.A. Maradudin, Nonlinear s-polarized surface plasmon polaritons. Solid State Commun. **52**(3), 293–297 (1984)
99. G. Stegeman, C. Seaton, J. Ariyasu, R. Wallis, A. Maradudin, Nonlinear electromagnetic waves guided by a single interface. J. Appl. Phys. **58**(7), 2453–2459 (1985)
100. G. Bachelier, J. Butet, I. Russier-Antoine, C. Jonin, E. Benichou, P.-F. Brevet, Origin of optical second-harmonic generation in spherical gold nanoparticles: Local surface and nonlocal bulk contributions. Phys. Rev. B **82**(23), 235403 (2010)
101. V. Ng, A.M. Warrier, J. Lin, D.J. Spence, J.E. Downes, D.W. Coutts, J.M. Dawes, Plasmonic second-harmonic generation in gold: lithium niobate thin films. J. Optical Soc. Am. B **35**(2), 302–307 (2018)
102. R.W. Boyd, Z. Shi, I. De Leon, The third-order nonlinear optical susceptibility of gold. Optics Commun. **326**, 74–79 (2014)
103. M. Sheik-Bahae, A.A. Said, T.-H. Wei, D.J. Hagan, E.W. Van Stryland, Sensitive measurement of optical nonlinearities using a single beam. IEEE J. Quantum Electron. **26**(4), 760–769 (1990)
104. A.R. Davoyan, I.V. Shadrivov, Y.S. Kivshar, Self-focusing and spatial plasmon-polariton solitons. Optics Express **17**(24), 21732–21737 (2009)

105. A. Marini, M. Conforti, G Della Valle, H. Lee, T.X. Tran, W. Chang, M. Schmidt, S. Longhi, P.S.J. Russell, F. Biancalana, Ultrafast nonlinear dynamics of surface plasmon polaritons in gold nanowires due to the intrinsic nonlinearity of metals. New J. Phys. **15**(1), 013033 (2013)
106. O. Lysenko, M. Bache, N. Olivier, A.V. Zayats, A. Lavrinenko, Nonlinear dynamics of ultrashort long-range surface plasmon polariton pulses in gold strip waveguides. ACS Photonics **3**(12), 2324–2329 (2016)
107. I. De Leon, J. Sipe, R.W. Boyd, Self-phase-modulation of surface plasmon polaritons. Phys. Rev. A **89**(1), 013855 (2014)
108. S. Afshar, T.M. Monro, A full vectorial model for pulse propagation in emerging waveguides with subwavelength structures part I: Kerr nonlinearity. Optics Express **17**(4), 2298–2318 (2009)
109. G. Li, C.M. de Sterke, S. Palomba, General analytic expression and numerical approach for the Kerr nonlinear coefficient of optical waveguides. Optics Lett. **42**(7), 1329–1332 (2017)
110. G.H.Y. Li, A. Tuniz, C.M. de Sterke, Establishing the nonlinear coefficient for extremely lossy waveguides. Optics Lett. **45**(18), 5041–5044 (2020)
111. S.-J. Im, K.-S. Ho, Q.-Q. Wang, A. Husakou, J. Herrmann, Nonlinearity of surface-plasmon polaritons in sub-wavelength metal nanowires. Optics Express **24**(6), 6162–6171 (2016)
112. O. Reshef, E. Giese, M.Z. Alam, I. De Leon, J. Upham, R.W. Boyd, Beyond the perturbative description of the nonlinear optical response of low-index materials. Optics Lett. **42**(16), 3225–3228 (2017)
113. A. Maslov, Rigorous calculation of the nonlinear Kerr coefficient for a waveguide using power-dependent dispersion modification. Optics Lett. **39**(15), 4396–4399 (2014)
114. A. Degiron, D.R. Smith, Nonlinear long-range plasmonic waveguides. Phys. Rev. A **82**(3), 033812 (2010)
115. M.M. Elsawy, G. Renversez, Exact calculation of the nonlinear characteristics of 2D isotropic and anisotropic waveguides. Optics Lett. **43**(11), 2446–2449 (2018)
116. A.R. Davoyan, I.V. Shadrivov, Y.S. Kivshar, Nonlinear plasmonic slot waveguides. Optics Express **16**(26), 21209–21214 (2008)
117. A.R. Davoyan, I.V. Shadrivov, Y.S. Kivshar, Symmetry breaking in plasmonic waveguides with metal nonlinearities. Optics Lett. **36**(6), 930–932 (2011)
118. M.Z. Alam, I. De Leon, R.W. Boyd, Large optical nonlinearity of indium tin oxide in its epsilon-near-zero region. Science **352**(6287), 795–797 (2016)
119. P. Guo, R.D. Schaller, L.E. Ocola, B.T. Diroll, J.B. Ketterson, R.P. Chang, Large optical nonlinearity of ito nanorods for sub-picosecond all-optical modulation of the full-visible spectrum. Nat. Commun. **7**, 12892 (2016)
120. R. Del Coso, J. Solis, Relation between nonlinear refractive index and third-order susceptibility in absorbing media. J. Optical Soc. Am. B **21**(3), 640–644 (2004)
121. D.D. Smith, Y. Yoon, R.W. Boyd, J.K. Campbell, L.A. Baker, R.M. Crooks, M. George, Z-scan measurement of the nonlinear absorption of a thin gold film. J. Appl. Phys. **86**(11), 6200–6205 (1999)
122. L. Yin, G.P. Agrawal, Impact of two-photon absorption on self-phase modulation in silicon waveguides. Optics Lett. **32**(14), 2031–2033 (2007)
123. M.M. Hossain, M.D. Turner, M. Gu, Ultrahigh nonlinear nanoshell plasmonic waveguide with total energy confinement. Optics Express **19**(24), 23800–23808 (2011)
124. C. Kern, M. Zürch, J. Petschulat, T. Pertsch, B. Kley, T. Käsebier, U. Hübner, C. Spielmann, Comparison of femtosecond laser-induced damage on unstructured vs. nano-structured Au-targets. Appl. Phys. A **104**(1), 15 (2011)
125. G. Li, C.M. De Sterke, S. Palomba, Fundamental limitations to the ultimate Kerr nonlinear performance of plasmonic waveguides. ACS Photonics **5**(3), 1034–1040 (2018)
126. D.E. Chang, A.S. Sørensen, E.A. Demler, M.D. Lukin, A single-photon transistor using nanoscale surface plasmons. Nat. Phys. **3**(11), 807–812 (2007)
127. M.P. Nielsen, X. Shi, P. Dichtl, S.A. Maier, R.F. Oulton, Giant nonlinear response at a plasmonic nanofocus drives efficient four-wave mixing. Science **358**(6367), 1179–1181 (2017)
128. G. Li, S. Palomba, C.M. de Sterke, Two-dimensional plasmonic waveguides for nanolasing and four-wave mixing. New J. Phys. **21**(10), 103004 (2019)
129. J.B. Khurgin, G. Sun, Plasmonic enhancement of the third order nonlinear optical phenomena: Figures of merit. Optics Express **21**(22), 27460–27480 (2013)
130. M.A. Nielsen, I. Chuang, Quantum computation and quantum information. (Cambridge University press, 2000)

131. A. Baron, S. Larouche, D.J. Gauthier, D.R. Smith, Scaling of the nonlinear response of the surface plasmon polariton at a metal/dielectric interface. J. Optical Soc. Am. B **32**(1), 9–14 (2015)
132. I.H. Malitson, Interspecimen comparison of the refractive index of fused silica. J. Optical Soc. Am. **55**(10), 1205–1209 (1965)
133. Q. Lin, J. Zhang, G. Piredda, R.W. Boyd, P.M. Fauchet, G.P. Agrawal, Dispersion of silicon nonlinearities in the near infrared region. Appl. Phys. Lett. **91**(2), 021111 (2007)
134. A. Baron, N. Dubreuil, P. Delaye, R. Frey, G.P. Agrawal, Raman amplification of optical pulses in silicon nanowaveguides: Impact of spectral broadening of pump pulses. J. Eur. Optical Soc. **6**, 11030 (2011)
135. K. Koynov, A. Bahtiar, T. Ahn, C. Bubeck, H.-H. Hörhold, Molecular weight dependence of birefringence of thin films of the conjugated polymer poly [2-methoxy-5-(2'-ethyl-hexyloxy)-1, 4-phenylenevinylene]. Appl. Phys. Lett. **84**(19), 3792–3794 (2004)
136. I. De Leon, Z. Shi, A.C. Liapis, R.W. Boyd, Measurement of the complex nonlinear optical response of a surface plasmon-polariton. Optics Lett. **39**(8), 2274–2277 (2014)
137. G. Boyd, Applications requirements for nonlinear-optical devices and the status of organic materials. J. Optical Soc. Am. B **6**(4), 685–692 (1989)
138. A. Baron, A. Ryasnyanskiy, N. Dubreuil, P. Delaye, Q.V. Tran, S. Combrié, A. de Rossi, R. Frey, G. Roosen, Light localization induced enhancement of third order nonlinearities in a gaas photonic crystal waveguide. Optics Express **17**(2), 552–557 (2009)
139. V.G. Kravets, F. Wu, G.H. Auton, Y. Tongcheng, I. Shinji, A.N. Grigorenko, Measurements of electrically tunable refractive index of MoS_2 monolayer and its usage in optical modulators. NPJ 2D Mater. Appl. **3**, 36 (2019)
140. R. Woodward, R. Murray, C. Phelan, R. De Oliveira, T. Runcorn, E. Kelleher, S. Li, E. De Oliveira, G. Fechine, G. Eda et al., Characterization of the second-and third-order nonlinear optical susceptibilities of monolayer mos2 using multiphoton microscopy. 2D Materials **4**(1), 011006 (2016)
141. J. Zhang, E. Cassan, D. Gao, X. Zhang, Highly efficient phase-matched second harmonic generation using an asymmetric plasmonic slot waveguide configuration in hybrid polymer-silicon photonics. Optics Express **21**(12), 14876–14887 (2013)
142. F. Lu, T. Li, X. Hu, Q. Cheng, S. Zhu, Y. Zhu, Efficient second-harmonic generation in nonlinear plasmonic waveguide. Optics Lett. **36**(17), 3371–3373 (2011)
143. J. Zhang, E. Cassan, X. Zhang, Efficient second harmonic generation from mid-infrared to near-infrared regions in silicon-organic hybrid plasmonic waveguides with small fabrication-error sensitivity and a large bandwidth. Optics Lett. **38**(12), 2089–2091 (2013)
144. T. Wu, P.P. Shum, X. Shao, T. Huang, Y. Sun, Third harmonic generation from mid-IR to near-IR regions in a phase-matched silicon-silicon-nanocrystal hybrid plasmonic waveguide. Optics Express **22**(20), 24367–24377 (2014)
145. K.F. MacDonald, Z.L. Sámson, M.I. Stockman, N.I. Zheludev, Ultrafast active plasmonics. Nat. Photonics **3**(1), 55–58 (2009)
146. M. Ono, M. Hata, M. Tsunekawa, K. Nozaki, H. Sumikura, H. Chiba, M. Notomi, Ultrafast and energy-efficient all-optical switching with graphene-loaded deep-subwavelength plasmonic waveguides. Nat. Photonics **14**(1), 37–43 (2020)
147. N. Rotenberg, A. Bristow, M. Pfeiffer, M. Betz, H. Van Driel, Nonlinear absorption in Au films: Role of thermal effects. Phys. Rev. B **75**(15), 155426 (2007)
148. A. Tuniz, S. Palomba, C.M. de Sterke, Pulse length dependent near-infrared ultrafast nonlinearity of gold by self-phase modulation. Appl. Phys. Lett. **117**(7), 071105 (2020)
149. A.V. Krasavin, P. Ginzburg, A.V. Zayats, Free-electron optical nonlinearities in plasmonic nanostructures: A review of the hydrodynamic description. Laser Photonics Rev. **12**(1), 1700082 (2018)
150. Y. Salamin, W. Heni, C. Haffner, Y. Fedoryshyn, C. Hoessbacher, R. Bonjour, M. Zahner, D. Hillerkuss, P. Leuchtmann, D.L. Elder et al., Direct conversion of free space millimeter waves to optical domain by plasmonic modulator antenna. Nano Lett. **15**(12), 8342–8346 (2015)
151. C. Haffner, W. Heni, Y. Fedoryshyn, J. Niegemann, A. Melikyan, D.L. Elder, B. Baeuerle, Y. Salamin, A. Josten, U. Koch et al., All-plasmonic Mach-Zehnder modulator enabling optical high-speed communication at the microscale. Nat. Photonics **9**(8), 525–528 (2015)
152. C. Koos, J. Leuthold, W. Freude, M. Kohl, L. Dalton, W. Bogaerts, A.L. Giesecke, M. Lauermann, A. Melikyan, S. Koeber et al., Silicon-organic hybrid (SOH) and plasmonic-organic hybrid (POH) integration. J. Lightw. Technol. **34**(2), 256–268 (2015)

153. W. Heni, Y. Kutuvantavida, C. Haffner, H. Zwickel, C. Kieninger, S. Wolf, M. Lauermann, Y. Fedoryshyn, A.F. Tillack, L.E. Johnson et al., Silicon-organic and plasmonic-organic hybrid photonics. ACS Photonics **4**(7), 1576–1590 (2017)
154. U. Koch, C. Uhl, H. Hettrich, Y. Fedoryshyn, C. Hoessbacher, W. Heni, B. Baeuerle, B.I. Bitachon, A monolithic bipolar CMOS electronic-plasmonic high-speed transmitter. Nat. Electron. **3**(6), 338–345 (2020)
155. B. Chen, R. Bruck, D. Traviss, A.Z. Khokhar, S. Reynolds, D.J. Thomson, G.Z. Mashanovich, G.T. Reed, O.L. Muskens, Hybrid photon-plasmon coupling and ultrafast control of nanoantennas on a silicon photonic chip. Nano Lett. **18**(1), 610–617 (2018)
156. P. Vaiano, B. Carotenuto, M. Pisco, A. Ricciardi, G. Quero, M. Consales, A. Crescitelli, E. Esposito, A. Cusano, Lab on fiber technology for biological sensing applications. Laser Photonics Rev. **10**(6), 922–961 (2016)
157. Y. Luo, M. Chamanzar, A. Apuzzo, R. Salas-Montiel, K.N. Nguyen, S. Blaize, A. Adibi, On-chip hybrid photonic-plasmonic light concentrator for nanofocusing in an integrated silicon photonics platform. Nano Lett. **15**(2), 849–856 (2015)
158. F. Diaz, T. Hatakeyama, J. Rho, Y. Wang, K. O'Brien, X. Zhang, C.M. de Sterke, B. Kuhlmey, S. Palomba, Sensitive method for measuring third order nonlinearities in compact dielectric and hybrid plasmonic waveguides. Optics Express **24**(1), 545–554 (2016)
159. H. Simon, D. Mitchell, J. Watson, Optical second-harmonic generation with surface plasmons in silver films. Phys. Rev. Lett. **33**(26), 1531 (1974)
160. N.B. Grosse, J. Heckmann, U. Woggon, Nonlinear plasmon-photon interaction resolved by k-space spectroscopy. Phys. Rev. Lett. **108**(13), 136802 (2012)
161. A.E. Bieber, D.F. Prelewitz, T.G. Brown, R.C. Tiberio, Nonlinear-optical interactions in metal-semiconductor-metal waveguide structures. J. Optical Soc. Am. B **13**(1), 34–40 (1996)
162. N. Rotenberg, M. Betz, H.M. van Driel, Ultrafast all-optical coupling of light to surface plasmon polaritons on plain metal surfaces. Phys. Rev. Lett. **105**(1), 017402 (2010)
163. J.N. Caspers, N. Rotenberg, H.M. van Driel, Ultrafast silicon-based active plasmonics at telecom wavelengths. Optics Express **18**(19), 19761–19769 (2010)
164. A.V. Krasavin, S. Randhawa, J.-S. Bouillard, J. Renger, R. Quidant, A.V. Zayats, Optically-programmable nonlinear photonic component for dielectric-loaded plasmonic circuitry. Optics Express **19**(25), 25222–25229 (2011)
165. S. Palomba, L. Novotny, Nonlinear excitation of surface plasmon polaritons by four-wave mixing. Phys. Rev. Lett. **101**(5), 056802 (2008)
166. S. Palomba, H. Harutyunyan, J. Renger, R. Quidant, N.F. van Hulst, L. Novotny, Nonlinear plasmonics at planar metal surfaces. Philos. Trans. R. Soc. A Math. Phys. Eng. Sci. **369**(1950), 3497–3509 (2011)
167. J. Renger, R. Quidant, N. Van Hulst, L. Novotny, Surface-enhanced nonlinear four-wave mixing. Phys. Rev. Lett. **104**(4), (2010)
168. P. Genevet, J.-P. Tetienne, E. Gatzogiannis, R. Blanchard, M.A. Kats, M.O. Scully, F. Capasso, Large enhancement of nonlinear optical phenomena by plasmonic nanocavity gratings. Nano Lett. **10**(12), 4880–4883 (2010)
169. A. Baron, T.B. Hoang, C. Fang, M.H. Mikkelsen, D.R. Smith, Ultrafast self-action of surface-plasmon polaritons at an air/metal interface. Phys. Rev. B **91**(19), 195412 (2015)
170. A. Tuniz, S. Weidlich, M.A. Schmidt, Effectively single-mode self-recovering ultrafast nonlinear nanowire surface plasmons. Phys. Rev. Appl. **9**(4), 044012 (2018)
171. G. Stegeman, J. Burke, D. Hall, Nonlinear optics of long range surface plasmons. Appl. Phys. Lett. **41**(10), 906–908 (1982)
172. J. Quail, J. Rako, H. Simon, R. Deck, Optical second-harmonic generation with long-range surface plasmons. Phys. Rev. Lett. **50**(25), 1987 (1983)
173. O. Lysenko, M. Bache, A. Lavrinenko, Third-order susceptibility of gold for ultrathin layers. Optics Lett. **41**(2), 317–320 (2016)
174. H. Qian, Y. Xiao, Z. Liu, Giant Kerr response of ultrathin gold films from quantum size effect. Nat. Commun. **7**, 13153 (2016)
175. H. Lee, M. Schmidt, R. Russell, N. Joly, H. Tyagi, P. Uebel, P.S.J. Russell, Pressure-assisted melt-filling and optical characterization of Au nano-wires in microstructured fibers. Optics Express **19**(13), 12180–12189 (2011)
176. A. de Hoogh, A. Opheij, M. Wulf, N. Rotenberg, L. Kuipers, Harmonics generation by surface plasmon polaritons on single nanowires. ACS Photonics **3**(8), 1446–1452 (2016)

177. E. Verhagen, L. Kuipers, A. Polman, Enhanced nonlinear optical effects with a tapered plasmonic waveguide. Nano Lett. **7**(2), 334–337 (2007)
178. T.-Y. Chen, J. Obermeier, T. Schumacher, F.-C. Lin, J.-S. Huang, M. Lippitz, C.-B. Huang, Modal symmetry controlled second-harmonic generation by propagating plasmons. Nano Lett. **19**(9), 6424–6428 (2019)
179. I.-Y. Park, S. Kim, J. Choi, D.-H. Lee, Y.-J. Kim, M.F. Kling, M.I. Stockman, S.-W. Kim, Plasmonic generation of ultrashort extreme-ultraviolet light pulses. Nat. Photonics **5**(11), 677–681 (2011)
180. V. Kravtsov, R. Ulbricht, J.M. Atkin, M.B. Raschke, Plasmonic nanofocused four-wave mixing for femtosecond near-field imaging. Nat. Nanotechnol. **11**(5), 459–464 (2016)
181. S. Berweger, J.M. Atkin, X.G. Xu, R.L. Olmon, M.B. Raschke, Femtosecond nanofocusing with full optical waveform control. Nano Lett. **11**(10), 4309–4313 (2011)
182. J. Vogelsang, J. Robin, B.J. Nagy, P. Dombi, D. Rosenkranz, M. Schiek, P. Groß, C. Lienau, Ultrafast electron emission from a sharp metal nanotaper driven by adiabatic nanofocusing of surface plasmons. Nano Lett. **15**(7), 4685–4691 (2015)
183. V. Kravtsov, S. AlMutairi, R. Ulbricht, A.R. Kutayiah, A. Belyanin, M.B. Raschke, Enhanced third-order optical nonlinearity driven by surface-plasmon field gradients. Phys. Rev. Lett. **120**(20), 203903 (2018)
184. P. Dombi, Z. Pápa, J. Vogelsang, S.V. Yalunin, M. Sivis, G. Herink, S. Schäfer, P. Groß, C. Ropers, C. Lienau, Strong-field nano-optics. Rev. Mod. Phys. **92**(2), 025003 (2020)
185. S. Sederberg, A. Elezzabi, Coherent visible-light-generation enhancement in silicon-based nanoplasmonic waveguides via third-harmonic conversion. Phys. Rev. Lett. **114**(22), 227401 (2015)
186. F.J. Rodríguez-Fortuño, A. Espinosa-Soria, A. Martínez, Exploiting metamaterials, plasmonics and nanoantennas concepts in silicon photonics. J. Optics **18**(12), 123001 (2016)
187. S. Sederberg, C.J. Firby, S.R. Greig, A.Y. Elezzabi, Integrated nanoplasmonic waveguides for magnetic, nonlinear, and strong-field devices. Nanophotonics **6**(1), 235–257 (2017)
188. J. Shi, Y. Li, M. Kang, X. He, N.J. Halas, P. Nordlander, S. Zhang, H. Xu, Efficient second harmonic generation in a hybrid plasmonic waveguide by mode interactions. Nano Lett. **19**(6), 3838–3845 (2019)
189. Z. Li, B. Corbett, A. Gocalinska, E. Pelucchi, W. Chen, K.M. Ryan, P. Khan, C. Silien, H. Xu, N. Liu, Direct visualization of phase-matched efficient second harmonic and broadband sum frequency generation in hybrid plasmonic nanostructures. Light Sci. Appl. **9**, 180 (2020)
190. T. Kuriakose, G. Renversez, V. Nazabal, M.M. Elsawy, N. Coulon, P. Nemec, M. Chauvet, Nonlinear self-confined plasmonic beams: experimental proof. ACS Photonics **7**(9), 2562–2570 (2020)
191. T.J. Duffin, M.P. Nielsen, F. Diaz, S. Palomba, S.A. Maier, R.F. Oulton, Degenerate four-wave mixing in silicon hybrid plasmonic waveguides. Optics Lett. **41**(1), 155–158 (2016)
192. J.R. Salgueiro, Y.S. Kivshar, Nonlinear plasmonic directional couplers. Appl. Phys. Lett. **97**(8), (2010)
193. A. Kriesch, D. Ploss, J. Wen, U. Peschel, Nonlinear switching in a purely plasmonic directional coupler. in *Signal Processing in Photonic Communications* (Optical Society of America, 2012), pp. JM5A–47
194. A. Melikyan, L. Alloatti, A. Muslija, D. Hillerkuss, P.C. Schindler, J. Li, R. Palmer, D. Korn, S. Muehlbrandt, D. Van Thourhout et al., High-speed plasmonic phase modulators. Nat. Photonics **8**(3), 229–233 (2014)
195. Z. Han, A. Elezzabi, V. Van, Experimental realization of subwavelength plasmonic slot waveguides on a silicon platform. Optics Lett. **35**(4), 502–504 (2010)
196. L. Lafone, T.P. Sidiropoulos, R.F. Oulton, Silicon-based metal-loaded plasmonic waveguides for low-loss nanofocusing. Optics Lett. **39**(15), 4356–4359 (2014)
197. O. Reshef, I. De Leon, M.Z. Alam, R.W. Boyd, Nonlinear optical effects in epsilon-near-zero media. Nat. Rev. Mater. **4**(8), 535–551 (2019)
198. L. Caspani, R. Kaipurath, M. Clerici, M. Ferrera, T. Roger, J. Kim, N. Kinsey, M. Pietrzyk, A. Di Falco, V.M. Shalaev et al., Enhanced nonlinear refractive index in ε-near-zero materials. Phys. Rev. Lett. **116**(23), 233901 (2016)
199. A.D. Neira, N. Olivier, M.E. Nasir, W. Dickson, G.A. Wurtz, A.V. Zayats, Eliminating material constraints for nonlinearity with plasmonic metamaterials. Nat. Commun. **6**, 7757 (2015)
200. J. Bohn, T.-S. Luk, C. Tollerton, S. Hutchins, I. Brener, S. Horsley, W. Barnes, E. Hendry, All-optical switching of an epsilon-near-zero plasmon in ITO. Nat. Commun. **12**, 1017 (2021)
201. S. Campione, I. Brener, F. Marquier, Theory of epsilon-near-zero modes in ultrathin films. Phys. Rev. B **91**(12), 121408(R) (2015)

202. S. Vassant, J.-P. Hugonin, F. Marquier, J.-J. Greffet, Berreman mode and epsilon near zero mode. Optics Express **20**(21), 23971–23977 (2012)
203. S. Campione, I. Kim, D. de Ceglia, G.A. Keeler, T.S. Luk, Experimental verification of epsilon-near-zero plasmon polariton modes in degenerately doped semiconductor nanolayers. Optics Express **24**(16), 18782–18789 (2016)
204. K. Minn, A. Anopchenko, J. Yang, H.W.H. Lee, Excitation of epsilon-near-zero resonance in ultra-thin indium tin oxide shell embedded nanostructured optical fiber. Sci. Rep. **8**(1), 2342 (2018)
205. C. Argyropoulos, P.-Y. Chen, G. D'Aguanno, N. Engheta, A. Alu, Boosting optical nonlinearities in ε-near-zero plasmonic channels. Phys. Rev. B **85**(4), 045129 (2012)
206. Y. Li, C. Argyropoulos, Exceptional points and spectral singularities in active epsilon-near-zero plasmonic waveguides. Phys. Rev. B **99**(7), 075413 (2019)
207. Y. Li, C. Argyropoulos, Epsilon-near-zero plasmonic waveguides to enhance nonlinear coherent light-matter interactions. Active Photonic Platf. X **10721**, 1072106 (2018)
208. T.S. Luk, D. De Ceglia, S. Liu, G.A. Keeler, R.P. Prasankumar, M.A. Vincenti, M. Scalora, M.B. Sinclair, S. Campione, Enhanced third harmonic generation from the epsilon-near-zero modes of ultrathin films. Appl. Phys. Lett. **106**(15), 151103 (2015)
209. A. Tuniz, O. Bickerton, F.J. Diaz, T. Käsebier, E.-B. Kley, S. Kroker, S. Palomba, C.M. de Sterke, Modular nonlinear hybrid plasmonic circuit. Nat. Commun. **11**, 2413 (2020)
210. E. Hendry, P.J. Hale, J. Moger, A. Savchenko, S.A. Mikhailov, Coherent nonlinear optical response of graphene. Phys. Rev. Lett. **105**(9), 097401 (2010)
211. M. Ono, H. Taniyama, H. Xu, M. Tsunekawa, E. Kuramochi, K. Nozaki, M. Notomi, Deep-subwavelength plasmonic mode converter with large size reduction for si-wire waveguide. Optica **3**(9), 999–1005 (2016)
212. B. Yao, Y. Liu, S.-W. Huang, C. Choi, Z. Xie, J.F. Flores, Y. Wu, M. Yu, D.-L. Kwong, Y. Huang et al., Broadband gate-tunable terahertz plasmons in graphene heterostructures. Nat. Photonics **12**(1), 22–28 (2018)
213. J.A. Dionne, K. Diest, L.A. Sweatlock, H.A. Atwater, PlasMOStor: a metal-oxide-Si field effect plasmonic modulator. Nano Lett. **9**(2), 897–902 (2009)
214. F. Ren, X. Wang, A.X. Wang, Thermo-optic modulation of plasmonic bandgap on metallic photonic crystal slab. Appl. Phys. Lett. **102**(18), 181101 (2013)
215. S. Randhawa, S. Lachèze, J. Renger, A. Bouhelier, R.E. de Lamaestre, A. Dereux, R. Quidant, Performance of electro-optical plasmonic ring resonators at telecom wavelengths. Optics Express **20**(3), 2354–2362 (2012)
216. M. Ayata, Y. Fedoryshyn, W. Heni, B. Baeuerle, A. Josten, M. Zahner, U. Koch, Y. Salamin, C. Hoessbacher, C. Haffner et al., High-speed plasmonic modulator in a single metal layer. Science **358**(6363), 630–632 (2017)
217. C. Haffner, D. Chelladurai, Y. Fedoryshyn, A. Josten, B. Baeuerle, W. Heni, T. Watanabe, T. Cui, B. Cheng, S. Saha et al., Low-loss plasmon-assisted electro-optic modulator. Nature **556**(7702), 483–486 (2018)
218. P.U. Jepsen, D.G. Cooke, M. Koch, Terahertz spectroscopy and imaging-modern techniques and applications. Laser Photonics Rev. **5**(1), 124–166 (2011)
219. M. Burla, C. Hoessbacher, W. Heni, C. Haffner, Y. Fedoryshyn, D. Werner, T. Watanabe, H. Massler, D.L. Elder, L.R. Dalton et al., 500 GHz plasmonic Mach-Zehnder modulator enabling sub-THz microwave photonics. APL Photonics **4**(5), 056106 (2019)
220. Y. Salamin, I.-C. Benea-Chelmus, Y. Fedoryshyn, W. Heni, D.L. Elder, L.R. Dalton, J. Faist, J. Leuthold, Compact and ultra-efficient broadband plasmonic terahertz field detector. Nat. Commun. **10**, 5550 (2019)
221. Y. Salamin, B. Baeuerle, W. Heni, F.C. Abrecht, A. Josten, Y. Fedoryshyn, C. Haffner, R. Bonjour, T. Watanabe, M. Burla et al., Microwave plasmonic mixer in a transparent fibre–wireless link. Nat. Photonics **12**(12), 749–753 (2018)
222. S. Ummethala, T. Harter, K. Koehnle, Z. Li, S. Muehlbrandt, Y. Kutuvantavida, J. Kemal, P. Marin-Palomo, J. Schaefer, A. Tessmann et al., THz-to-optical conversion in wireless communications using an ultra-broadband plasmonic modulator. Nat. Photonics **13**(8), 519–524 (2019)
223. A. Schneider, M. Neis, M. Stillhart, B. Ruiz, R.U. Khan, P. Günter, Generation of terahertz pulses through optical rectification in organic dast crystals: theory and experiment. J. Optical Soc. Am. B **23**(9), 1822–1835 (2006)

224. M. Jazbinsek, U. Puc, A. Abina, A. Zidansek, Organic crystals for THz photonics. Appl. Sci. **9**(5), 882 (2019)
225. F. Kadlec, P. Kužel, J.-L. Coutaz, Optical rectification at metal surfaces. Optics Lett. **29**(22), 2674–2676 (2004)
226. D. Polyushkin, E. Hendry, E. Stone, W. Barnes, THz generation from plasmonic nanoparticle arrays. Nano Lett. **11**(11), 4718–4724 (2011)
227. L. Luo, I. Chatzakis, J. Wang, F.B. Niesler, M. Wegener, T. Koschny, C.M. Soukoulis, Broadband terahertz generation from metamaterials. Nat. Commun. **5**, 3055 (2014)
228. J. Langer, D. Jimenez de Aberasturi, J. Aizpurua, R.A. Alvarez-Puebla, B. Auguié, J.J. Baumberg, G.C. Bazan, S.E. Bell, A. Boisen, A.G. Brolo et al., Present and future of surface-enhanced Raman scattering. ACS Nano **14**(1), 28–117 (2019)
229. A.X. Wang, X. Kong, Review of recent progress of plasmonic materials and nano-structures for surface-enhanced Raman scattering. Materials **8**(6), 3024–3052 (2015)
230. D.M. Solís, J.M. Taboada, F. Obelleiro, L.M. Liz-Marzán, F.J. García de Abajo, Optimization of nanoparticle-based sers substrates through large-scale realistic simulations. ACS Photonics **4**(2), 329–337 (2017)
231. Y. Fang, H. Wei, F. Hao, P. Nordlander, H. Xu, Remote-excitation surface-enhanced Raman scattering using propagating Ag nanowire plasmons. Nano Lett. **9**(5), 2049–2053 (2009)
232. J.A. Hutchison, S.P. Centeno, H. Odaka, H. Fukumura, J. Hofkens, H. Uji-i, Subdiffraction limited, remote excitation of surface enhanced raman scattering. Nano Lett. **9**(3), 995–1001 (2009)
233. G. Lu, H. De Keersmaecker, L. Su, B. Kenens, S. Rocha, E. Fron, C. Chen, P. Van Dorpe, H. Mizuno, J. Hofkens et al., Live-cell sers endoscopy using plasmonic nanowire waveguides. Adv. Mater. **26**(30), 5124–5128 (2014)
234. K. Tomita, Y. Kojima, F. Kannari, Selective coherent anti-stokes raman scattering microscopy employing dual-wavelength nanofocused ultrafast plasmon pulses. Nano Lett. **18**(2), 1366–1372 (2018)
235. F. Peyskens, P. Wuytens, A. Raza, P. Van Dorpe, R. Baets, Waveguide excitation and collection of surface-enhanced raman scattering from a single plasmonic antenna. Nanophotonics **7**(7), 1299–1306 (2018)
236. A. Raza, S. Clemmen, P. Wuytens, M. Muneeb, M. Van Daele, J. Dendooven, C. Detavernier, A. Skirtach, R. Baets, ALD assisted nanoplasmonic slot waveguide for on-chip enhanced Raman spectroscopy. APL Photonics **3**(11), 116105 (2018)
237. Y. Li, H. Zhao, A. Raza, S. Clemmen, R. Baets, Surface-enhanced Raman spectroscopy based on plasmonic slot waveguides with free-space oblique illumination. IEEE J. Quantum Electron. **56**(1), 7200108 (2019)
238. T. Rudolph, Why I am optimistic about the silicon-photonic route to quantum computing. APL Photonics **2**(3), 030901 (2017)
239. N. Gisin, G. Ribordy, W. Tittel, H. Zbinden, Quantum cryptography. Reviews of Modern Physics **74**(1), 145 (2002)
240. V. Giovannetti, S. Lloyd, L. Maccone, Advances in quantum metrology. Nat. Photonics **5**(4), 222–229 (2011)
241. J.F. Clauser, M.A. Horne, A. Shimony, R.A. Holt, Proposed experiment to test local hidden-variable theories. Phys. Rev. Lett. **23**(15), 880 (1969)
242. S.J. Freedman, J.F. Clauser, Experimental test of local hidden-variable theories. Phys. Rev. Lett. **28**(14), 938 (1972)
243. J.L. O'Brien, A. Furusawa, J. Vučković, Photonic quantum technologies. Nat. Photonics **3**(12), 687–695 (2009)
244. L. Caspani, C. Xiong, B.J. Eggleton, D. Bajoni, M. Liscidini, M. Galli, R. Morandotti, D.J. Moss, Integrated sources of photon quantum states based on nonlinear optics. Light Sci. Appl. **6**(11), e17100 (2017)
245. I. d'Amico, D. Angelakis, F. Bussieres, H. Caglayan, C. Couteau, T. Durt, B. Kolaric, P. Maletinsky, W. Pfeiffer, P. Rabl et al., Nanoscale quantum optics. La Riv. del Nuovo Cim. **42**, 153–195 (2019)
246. D.E. Chang, V. Vuletić, M.D. Lukin, Quantum nonlinear optics-photon by photon. Nat. Photonics **8**(9), 685–694 (2014)
247. T. Volz, A. Reinhard, M. Winger, A. Badolato, K.J. Hennessy, E.L. Hu, A. Imamoğlu, Ultrafast all-optical switching by single photons. Nat. Photonics **6**(9), 605–609 (2012)
248. W. Chen, K.M. Beck, R. Bücker, M. Gullans, M.D. Lukin, H. Tanji-Suzuki, V. Vuletić, All-optical switch and transistor gated by one stored photon. Science **341**(6147), 768–770 (2013)

249. A. Reiserer, N. Kalb, G. Rempe, S. Ritter, A quantum gate between a flying optical photon and a single trapped atom. Nature **508**(7495), 237–240 (2014)
250. S. Mahmoodian, G. Calajó, D.E. Chang, K. Hammerer, A.S. Sørensen, Dynamics of many-body photon bound states in chiral waveguide QED. Phys. Rev. X **10**(3), 031011 (2020)
251. A.G. Curto, G. Volpe, T.H. Taminiau, M.P. Kreuzer, R. Quidant, N.F. van Hulst, Unidirectional emission of a quantum dot coupled to a nanoantenna. Science **329**(5994), 930–933 (2010)
252. J.T. Hugall, A. Singh, N.F. van Hulst, Plasmonic cavity coupling. ACS Photonics **5**(1), 43–53 (2018)
253. D. Chang, A.S. Sørensen, P. Hemmer, M. Lukin, Quantum optics with surface plasmons. Phys. Rev. Lett. **97**(5), 053002 (2006)
254. P. Lodahl, S. Mahmoodian, S. Stobbe, Interfacing single photons and single quantum dots with photonic nanostructures. Rev. Mod. Phys. **87**(2), 347 (2015)
255. H. Siampour, S. Kumar, V.A. Davydov, L.F. Kulikova, V.N. Agafonov, S.I. Bozhevolnyi, On-chip excitation of single germanium vacancies in nanodiamonds embedded in plasmonic waveguides. Light Sci. Appl. **7**(1), 61 (2018)
256. S.I. Bozhevolnyi, J.B. Khurgin, Fundamental limitations in spontaneous emission rate of single-photon sources. Optica **3**(12), 1418–1421 (2016)
257. M.S. Tame, K. McEnery, Ş. Özdemir, J. Lee, S.A. Maier, M. Kim, Quantum plasmonics. Nat. Phys. **9**(6), 329–340 (2013)
258. D. Xu, X. Xiong, L. Wu, X.-F. Ren, C.E. Png, G.-C. Guo, Q. Gong, Y.-F. Xiao, Quantum plasmonics: new opportunity in fundamental and applied photonics. Adv. Optics Photonics **10**(4), 703–756 (2018)
259. S.I. Bozhevolnyi, J.B. Khurgin, The case for quantum plasmonics. Nat. Photonics **11**(7), 398–400 (2017)
260. A.I. Fernández-Domínguez, S.I. Bozhevolnyi, N.A. Mortensen, Plasmon-enhanced generation of nonclassical light. ACS Photonics **5**(9), 3447–3451 (2018)
261. P. Türschmann, H. Le Jeannic, S.F. Simonsen, H.R. Haakh, S. Götzinger, V. Sandoghdar, P. Lodahl, N. Rotenberg, Coherent nonlinear optics of quantum emitters in nanophotonic waveguides. Nanophotonics **8**(10), 1641–1657 (2019)
262. S.I. Bogdanov, A. Boltasseva, V.M. Shalaev, Overcoming quantum decoherence with plasmonics. Science **364**(6440), 532–533 (2019)
263. S. Wein, N. Lauk, R. Ghobadi, C. Simon, Feasibility of efficient room-temperature solid-state sources of indistinguishable single photons using ultrasmall mode volume cavities. Phys. Rev. B **97**(20), 205418 (2018)
264. C. Schörner, M. Lippitz, Single molecule nonlinearity in a plasmonic waveguide. Nano Lett. **20**(3), 2152–2156 (2020)
265. S. Grandi, M.P. Nielsen, J. Cambiasso, S. Boissier, K.D. Major, C. Reardon, T.F. Krauss, R.F. Oulton, E. Hinds, A.S. Clark, Hybrid plasmonic waveguide coupling of photons from a single molecule. APL Photonics **4**(8), 086101 (2019)
266. M.R. Rosenberger, C.K. Dass, H.-J. Chuang, S.V. Sivaram, K.M. McCreary, J.R. Hendrickson, B.T. Jonker, Quantum calligraphy: writing single-photon emitters in a two-dimensional materials platform. ACS Nano **13**(1), 904–912 (2019)
267. S. Luo, A. Mancini, R. Berté, B.H. Hoff, S.A. Maier, J. de Mello, Fabrication of size-controlled metallic nanogaps down to the sub 3-nm level (2020). https://chemrxiv.org/articles/preprint/Fabrication_of_Size-Controlled_Metallic_Nanogaps_down_to_the_Sub_3-Nm_Level/13158173. https://doi.org/10.26434/chemrxiv.13158173.v1
268. S.-H. Gong, J.-H. Kim, Y.-H. Ko, C. Rodriguez, J. Shin, Y.-H. Lee, L.S. Dang, X. Zhang, Y.-H. Cho, Self-aligned deterministic coupling of single quantum emitter to nanofocused plasmonic modes. Proc. Natl. Acad. Sci. **112**(17), 5280–5285 (2015)
269. A.N. Poddubny, I.V. Iorsh, A.A. Sukhorukov, Generation of photon-plasmon quantum states in nonlinear hyperbolic metamaterials. Phys. Rev. Lett. **117**(12), 123901 (2016)
270. M. Difallah, A. Szameit, M. Ornigotti, Path-integral description of quantum nonlinear optics in arbitrary media. Phys. Rev. A **100**(5), 053845 (2019)
271. Y. Ming, W. Zhang, Z. Chen, Z. Wu, J. Tang, F. Xu, L. Zhang, Y. Lu, Squeezing a surface plasmon through quadratic nonlinear interactions. ACS Photonics **3**(11), 2074–2082 (2016)
272. A. Loot, V. Hizhnyakov, Modeling of enhanced spontaneous parametric down-conversion in plasmonic and dielectric structures with realistic waves. J. Optics **20**(5), 055502 (2018)

273. A. Loot, I. Sildos, V. Kiisk, T. Romann, V. Hizhnyakov, Steps toward the experimental realization of surface plasmon polariton enhanced spontaneous parametric down-conversion. Optik **171**, 557–564 (2018)
274. A. Grigorenko, M. Polini, K. Novoselov, Graphene plasmonics. Nat. Photonics **6**(11), 749–758 (2012)
275. W. Gao, G. Shi, Z. Jin, J. Shu, Q. Zhang, R. Vajtai, P.M. Ajayan, J. Kono, Q. Xu, Excitation and active control of propagating surface plasmon polaritons in graphene. Nano Lett. **13**(8), 3698–3702 (2013)
276. K.J. Ooi, J. Cheng, J. Sipe, L. Ang, D.T. Tan, Ultrafast, broadband, and configurable midinfrared all-optical switching in nonlinear graphene plasmonic waveguides. APL Photonics **1**(4), 046101 (2016)
277. Q. Feng, H. Cong, B. Zhang, W. Wei, Y. Liang, S. Fang, T. Wang, J. Zhang, Enhanced optical Kerr nonlinearity of graphene/Si hybrid waveguide. Appl. Phys. Lett. **114**(7), 071104 (2019)
278. Y. Li, M. Kang, J. Shi, K. Wu, S. Zhang, H. Xu, Transversely divergent second harmonic generation by surface plasmon polaritons on single metallic nanowires. Nano Lett. **17**(12), 7803–7808 (2017)
279. C. Ciracì, R.T. Hill, J.J. Mock, Y. Urzhumov, A.I. Fernández-Domínguez, S.A. Maier, J.B. Pendry, A. Chilkoti, D.R. Smith, Probing the ultimate limits of plasmonic enhancement. Science **337**(6098), 1072–1074 (2012)
280. X. Li, J. Zhu, B. Wei, Hybrid nanostructures of metal/two-dimensional nanomaterials for plasmon-enhanced applications. Chem. Soc. Rev. **45**(11), 3145–3187 (2016)
281. S. Yan, X. Zhu, J. Dong, Y. Ding, S. Xiao, 2D materials integrated with metallic nanostructures: fundamentals and optoelectronic applications. Nanophotonics **9**(7), 1299–1306 (2018)
282. N. Flöry, P. Ma, Y. Salamin, A. Emboras, T. Taniguchi, K. Watanabe, J. Leuthold, L. Novotny, Waveguide-integrated van der waals heterostructure photodetector at telecom wavelengths with high speed and high responsivity. Nat. Nanotechnol. **15**(2), 118–124 (2020)
283. G.Q. Ngo, A. George, R.T.K. Schock, A. Tuniz, E. Najafidehaghani, Z. Gan, N.C. Geib, T. Bucher, H. Knopf, S. Saravi, C. Neumann, T. Lühder, E.P. Schartner, S.C. Warren-Smith, H. Ebendorff-Heidepriem, T. Pertsch, M.A. Schmidt, A. Turchanin, F. Eilenberger, Scalable functionalization of optical fibers using atomically thin semiconductors. Adv. Mater. **32**(47), 2003826 (2020)
284. Y. Zuo, W. Yu, C. Liu, X. Cheng, R. Qiao, J. Liang, X. Zhou, J. Wang, M. Wu, Y. Zhao et al., Optical fibres with embedded two-dimensional materials for ultrahigh nonlinearity. Nat. Nanotechnol. **15**(12), 987–991 (2020)
285. M.-A. Miri, A. Alu, Exceptional points in optics and photonics. Science **363**(6422), eaar7709 (2019)
286. A. Tuniz, T. Wieduwilt, M.A. Schmidt, Tuning the effective PT phase of plasmonic eigenmodes. Phys. Rev. Lett. **123**(21), 213903 (2019)
287. S.A.H. Gangaraj, F. Monticone, Topological waveguiding near an exceptional point: defect-immune, slow-light, and loss-immune propagation. Phys. Rev. Lett. **121**(9), 093901 (2018)
288. J.-H. Park, A. Ndao, W. Cai, L. Hsu, A. Kodigala, T. Lepetit, Y.-H. Lo, B. Kanté, Symmetry-breaking-induced plasmonic exceptional points and nanoscale sensing. Nat. Phys. **16**(4), 462–468 (2020)
289. V.V. Konotop, J. Yang, D.A. Zezyulin, Nonlinear waves in PT-symmetric systems. Rev. Mod. Phys. **88**(3), 035002 (2016)